Variation of the electronic states of Ca_2RuO_4 and Sr_2RuO_4 under uniaxial pressures

Ph.D Thesis
2014

**Department of Physics, Graduate School of Science,
Kyoto University, Kyoto, Japan**

Haruka TANIGUCHI

Abstract

Competition and cooperation among spin, orbital, and lattice degrees of freedom are key concepts to understand intriguing phenomena in condensed matter systems. As one of such fascinating systems, the layered perovskite ruthenates $Ca_{2-x}Sr_xRuO_4$ have been attracting wide interest for their variety of electronic states originating from multiple degrees of freedom: for example, Ca_2RuO_4 is an antiferromagnetic (AFM) Mott insulator, whereas Sr_2RuO_4 is a leading candidate for a spin-triplet superconductor.

For studying a system like $Ca_{2-x}Sr_xRuO_4$which has orbital degree of freedom, uniaxial pressure (UAP) is expected to be effective because it will couple well with orbital which spatially spreads along a certain direction. UAP can realize different crystal structures depending on pressure direction and intentionally control the symmetry of the crystal differently from hydrostatic pressure.

Therefore, we have studied the electronic states of Ca_2RuO_4 and Sr_2RuO_4 under UAPs with three different pressure directions: two in-plane directions, $[100]_T$ and $[110]_T$, and the out-of-plane direction, $[001]_T$, using the tetragonal notation. $[100]_T$ and $[110]_T$ direction are parallel and diagonal to the in-plane Ru-O bond of the RuO_6 octahedra, respectively.

For revealing the in-plane UAP effect on Ca_2RuO_4, we performed magnetization and resistivity measurements. We succeeded in inducing the ferromagnetic metallic (FM-M) phase. The mechanism of this Mott transition is considered to be the same as that under hydrostatic pressure: the out-of-plane flattening distortion of RuO_6 octahedra is released, and the *xy* and *yz,zx* bands of Ru 4*d* electrons approach energetically and overlap. The critical pressures of the FM-M phase for the UAPs (0.4 GPa for $P_{\parallel[100]T}$ and 0.2 GPa for $P_{\parallel[110]T}$) are substantially lower than that for the hydrostatic pressure (0.5 GPa). Interestingly, the critical pressure of the FM-M phase and the pressure dependence of FM component of magnetization were found to be highly anisotropic. These peculiar anisotropic results can be naturally understood as a consequence of the orthorhombic crystal distortions in Ca_2RuO_4 and existence of orthorhombic crystalline twin domains in the sample.

Surprisingly, the out-of-plane UAP effect on Ca_2RuO_4 was opposite to a simple prediction; from resistivity measurements, we have clarified that the insulating gap is suppressed from 3000 K to 700 K. This result suggests that Ca_2RuO_4 approaches a metallic state under the out-of-plane UAP with a mechanism, which is different from that of the Mott transition under in-plane UAP. Since the crystalline field splitting between the *xy* and *yz,zx* bands should become larger, this gap suppression is expected to be induced by the enhancement of the band width as a result of the release of rotation or/and tilting distortion of RuO_6 octahedra.

In the study of the out-of-plane UAP effect on the superconductivity (SC) of Sr_2RuO_4, we used Sr_2RuO_4-Ru eutectic crystals in order to compare the UAP-originated 3-K SC with the interfacial 3-K SC in the same sample. We previously revealed that the onset of superconducting transition temperature T_c of Sr_2RuO_4 without Ru inclusions is enhanced from 1.5 K to 3.2 K, which is the same as the onset T_c of the SC realized near interfaces between Sr_2RuO_4 and Ru in the eutectic crystal. In this thesis, we newly proposed the out-of-plane UAP dependence of the spatial distribution of 3-K SC in Sr_2RuO_4-Ru from AC susceptibility and resistivity measurements.

The in-plane UAP effect on Sr_2RuO_4 was also revealed to be significantly anisotropic from AC susceptibility measurements; we clarified that $P_{\parallel[100]\mathrm{T}}$ rather than $P_{\parallel[110]\mathrm{T}}$ is favorable for inducing 3-K SC.

Our results strongly demonstrate the effectiveness of UAP to control the electronic state of systems which have multiple degrees of freedom.

Contents

List of Figures

Chapter 1

Introduction

1.1 Motivation of the uniaxial pressure study of ruthenates

1.1.1 Background

Competition and cooperation among spin, orbital, and lattice degrees of freedom are key concepts to understand intriguing phenomena in condensed matter systems. As one of such fascinating systems, the layered perovskite ruthenates $Ca_{2-x}Sr_xRuO_4$ have been attracting wide interest for their variety of electronic states originating from multiple degrees of freedom: For example, Ca_2RuO_4 is an A-centered antiferromagnetic (A-AFM) Mott insulator with the metal-insulator transition temperature T_{M-I} = 357 K and the A-AFM ordering temperature T_{A-AFM}= 110 K [1, 2], while Sr_2RuO_4 is a leading candidate for a spin-triplet superconductor with the transition temperature T_c = 1.5 K [3, 4].

For revealing the nature of interesting phenomena originating from orbital degree of freedom, ruthenates have ideal complexity and simplicity. The electronic state of ruthenates is determined by the four 4*d* electrons per one Ru ion. Because Ru is octahedrally surrounded by O ions, in the layered perovskite crystal structure, the energy degeneracy of *d* orbitals is partially removed and the two e_g orbitals ($x^2 - y^2$ and $3z^2 - r^2$) locate energetically much higher than the rest three t_{2g} orbitals (xy, yz, zx) as shown in Fig. 1.1. Since the Hund's coupling plays only minor roles in 4*d* electrons, the four electrons in Ru 4*d* orbitals occupy the three t_{2g} orbitals: all *xy*, *yz*, and *zx* orbitals should have one electron but there still is a freedom to which orbital the fourth electron is located. In other words, ruthenates have orbital degree of freedom. However, in case of ruthenates, the situation is not too complex. For comparison, cuprates A_2CuO_4 and iron pnictides $LaFeAsO_{1-x}F_x$, which exhibit high-transition-temperature superconductivity and fascinate many researchers, have no orbital degree of freedom and five orbital possibilities, respectively; While cuprates have one hole per one Cu ion and the hole always occupies $x^2 - y^2$ orbital, all the *d* orbitals of pnictides form their band at the Fermi energy.

It has been recognized that distortions of the RuO_6 octahedra are responsible for the variety of the electronic states of the ruthenates; the octahedra in Sr_2RuO_4 have no distortion, while those in Ca_2RuO_4 have three kinds of distortions: flattening, tilting and rotation along/from/around the *c*

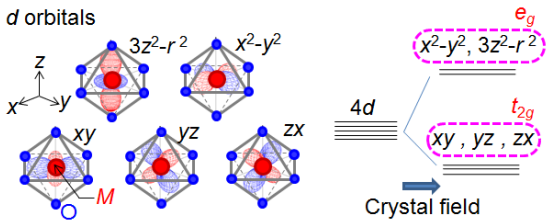

Figure 1.1: Orbitals of Ru 4*d* electrons in RuO_6 octahedra

axis [5]. These distortions in Ca_2RuO_4 are gradually removed by hydrostatic pressure (P_{hydro}) and the electronic state changes accordingly: At 0.2 GPa, the magnetic structure of the AFM phase changes from the A-AFM to the B-centered AFM (B-AFM) structure, accompanied by a partial release of the flattening [6, 7]. At 0.5 GPa, the flattening distortion is completely released and ferromagnetic metallic (FM-M) phase below the Curie temperature T_{FM} = 12-28 K appears [8, 6, 7]. At 10 GPa, the tilting distortion is released and superconductivity emerges [9]. Similar changes in the crystal structure and electronic state are observed also by substitution of Sr for Ca [10, 11, 12, 13]. Similarly, FM-M behavior is observed in Ca_2RuO_4 thin films, where in-plane epitaxial stress leads to a structural change [14, 15]. Recently-discovered electric-field-induced Mott transition in Ca_2RuO_4 is also accompanied by a change of the lattice distortion [16, 17]. Theoretical studies on relations between the lattice distortions and electronic states are also actively performed [18, 19, 20, 21, 22, 23, 24, 25, 26, 27, 28].

Moreover, T_c of Sr_2RuO_4 is also sensitive to lattice distortion: the enhancement of T_c up to 3 K is observed in Sr_2RuO_4-Ru eutectic crystals, where superconductivity with higher T_c occurs in the Sr_2RuO_4 part around Sr_2RuO_4-Ru interfaces as a consequence of the strong lattice distortion due to lattice mismatch [29, 30, 31]. We revealed that similar enhancement of T_c occurs in non-eutectic Sr_2RuO_4 under uniaxial pressure (UAP) [32]. In contrast, T_c of Sr_2RuO_4 is suppressed by P_{hydro} [33, 34]. In addition, double superconducting (SC) transitions are theoretically expected in Sr_2RuO_4 under in-plane UAP, because the SC order parameter of Sr_2RuO_4 is considered to consist of multiple components and the energy degeneracy of the components is expected to be removed by in-plane uniaxial pressure [35, 36].

1.1.2 Motivation

From these previous studies, it is expected that we can induce a wide variety of electronic states in $Ca_{2-x}Sr_xRuO_4$ by controlling the lattice distortion. As an effective method to control the lattice distortion, we focus on the following advantages of UAP. UAP can intentionally control the symmetry of the crystal differently from the application of hydrostatic pressure as shown in Fig. 1.2 and realize different crystal structures depending on pressure direction. These advantages mean that under UAP the variation of induced crystal structure is wider and systematic studies can be performed. Especially, for studying a system which has orbital degree of freedom, UAP is expected to be effective because it will couples well with orbital which spatially spreads along a certain direction.

However, UAP has also disadvantages: to achieve pressure homogeneity is rather difficult and

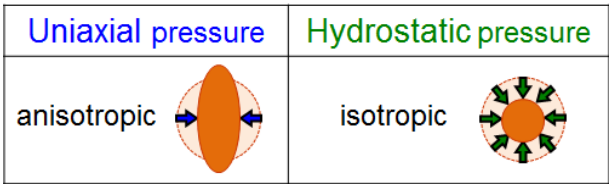

Figure 1.2: Comparison between uniaxial pressure and hydrostatic pressure

samples break easily. Thus, the technique of UAP experiments was not established yet, especially for oxides.

In my Ph. D study, we have first established the technique of UAP experiments, and then clarified UAP effects on Ca_2RuO_4 and Sr_2RuO_4.

Chapter 2

Fundamental properties of Ca_2RuO_4 and Sr_2RuO_4

2.1 Mott insulator Ca_2RuO_4

2.1.1 Coupling between the electronic state and the lattice distortion

The fundamental crystal structure of $Ca_{2-x}Sr_xRuO_4$ is of layered perovskite as shown in Fig. 2.1 (a). In Ca_2RuO_4, the RuO_6 octahedra have three kinds of lattice distortions: flattening, tilting and rotation along/from/about the c axis as shown in Fig. 2.2. In contrast, RuO_6 octahedra of Sr_2RuO_4 have no distortions. It is known that subtle lattice distortion strongly couples with the electronic state in this $Ca_{2-x}Sr_xRuO_4$ system. The ground state of Ca_2RuO_4 is an antiferromagnetic insulator (AFM-I), whereas that of Sr_2RuO_4 is a spin-triplet superconductor.

2.1.2 Sr substitution

In detail, three lattice distortions in $Ca_{2-x}Sr_xRuO_4$ is released as follows with increasing x, which reflects the proportion of Sr. The flattening distortion is released at $x = 0.2$ (Fig. 2.3) as a first-order phase transition. The ratio of Ru-O bond lengths (out-of-plane/in-plane) is 1.07 in Sr_2RuO_4 without the flattening, while it is 1.00 in Ca_2RuO_4 with the flattening, as shown in Fig. 2.1 (b) [5, 37]. Comparing with the ratio of Cu-O lengths of 1.26 in La_2CuO_4 [38], the flattening distortion of RuO_6 octahedra in Ca_2RuO_4 is significant. The tilting angle is gradually suppressed from 12° at $x = 0$ to 0° at $x = 0.5$ as shown in Fig. 2.4 [12]. While the tilting distortion exists, crystal symmetry is reduced from tetragonal to orthorhombic. The rotation angle remains constant (12°) up to $x = 0.5$, then gradually decreases, and becomes 0° at $x = 1.5$.

The ground state also changes drastically in $Ca_{2-x}Sr_xRuO_4$ by elemental substitution as shown in Fig. 2.5 [11]. Since Ca and Sr ions are isovalent in the crystal and the crystal structure is changed by Ca-Sr substitution, this variety of the ground states should originate from the difference in the crystal structure. It has been found that FM and AFM fluctuation are enhanced with increasing the rotation and tilting angle of RuO_6 octahedra, respectively. Also, the Mott transition and AFM order occur when the flattening distortion is induced. These results indicate that the

(a)

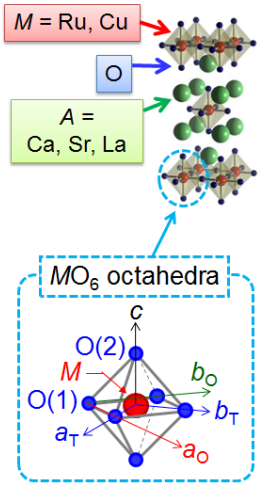

(b) @RoomT	M-O(1) (Å)	M-O(2) (Å)	M-O(2) / M-O(1) (out-of-plane / in-plane)
Ca_2RuO_4 (ambient)	1.990	1.995	1.00
Ca_2RuO_4 (1 GPa)	1.941	2.054	1.06
$Ca_{1.8}Sr_{0.2}RuO_4$	1.933	2.050	1.06
Sr_2RuO_4	1.935	2.066	1.07
La_2CuO_4	1.90	2.40	1.26

(c) @RoomT	a_O (Å)	b_O (Å)	c (Å)	a_O/b_O	c/a_O	c/b_O
Ca_2RuO_4 (ambient)	5.410	5.492	11.961	0.985	2.21	2.18
Ca_2RuO_4 (1 GPa)	5.331	5.316	12.292	1.00	2.31	2.31
Ca_2RuO_4 (thin film)	5.341	—	12.23	—	2.29	—
$Ca_{1.8}Sr_{0.2}RuO_4$	5.330	5.323	12.451	1.00	2.34	2.34
Sr_2RuO_4	5.474	5.474	12.740	1.00	2.33	2.33

Figure 2.1: (a) Crystal structure of A_2MO_4. (A: Alkaline earth metal, M: Transition metal) Subscripts "T" and "O" indicate "Tetragonal" and "Orthorhombic" notation, respectively. (b) In-plane and out-of-plane M-O bond lengths of A_2MO_4 under several conditions at room temperature. (c) Lattice constants in the orthorhombic notation of A_2MO_4 under several conditions at room temperature. The panels (b) and (c) are made based on Ref. [5, 6, 12, 37, 38, 39].

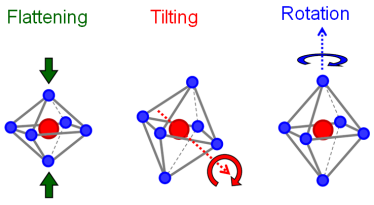

Figure 2.2: Lattice distortions of RuO_6 octahedra

ground state of $Ca_{2-x}Sr_xRuO_4$ indeed couples well with the lattice distortions of the RuO_6 octahedra. Theoretically, first principles calculation was performed with taking the magnitude of the lattice distortions as parameters as shown in Fig. 2.6 [19, 22]. This study revealed that the rotation and tilting induce ferromagnetism and antiferromagnetism, respectively, and the flattening forces them to order. Moreover, it is theoretically clarified that the band width is suppressed by any of these three distortions [40, 41, 42, 19, 22]. The possibility of orbital-selective Mott transition in this system is also an intriguing issue [21, 43].

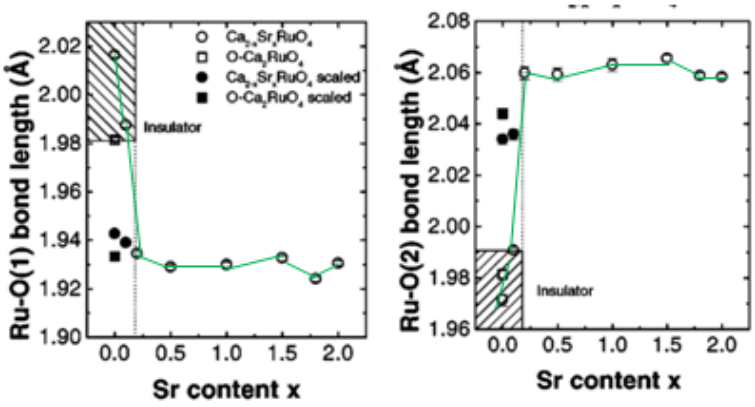

Figure 2.3: Sr-substitution dependence of Ru-O lengths in $Ca_{2-x}Sr_xRuO_4$ [12].

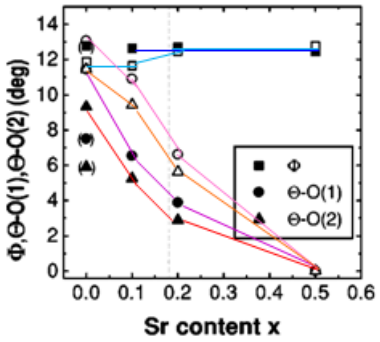

Figure 2.4: Sr-substitution dependence of the rotation angle Φ and the tilting angle θ of RuO_6 octahedra in $Ca_{2-x}Sr_xRuO_4$ [12].

2.1.3 Hydrostatic pressure

Hydrostatic pressure also induces the change of the electronic state of Ca_2RuO_4 which is similar to Sr substitution as shown in Fig. 2.7 [6, 9]. At 0.5 GPa, the flattening distortion is released as a first-order phase transition as shown in Fig. 2.8 (a) [6], and the electronic state becomes metal as shown in Fig. 2.8 (b) [8].

Hydrostatic pressure studies have also revealed that a transition to another AFM state, B-centered AFM (B-AFM) state, occurs at $T_{\mathrm{B-AFM}}$= 150 K between 0.2 and 0.8 GPa as shown in Fig. 2.7(a) [6, 7]. The B-AFM phase is realized also in Ca_2RuO_4 synthesized with the process of oxygen annealing [5]. In both cases, the flattening distortion of RuO_6 octahedra is partially released in the B-AFM phase.

The essential difference between the A- and B-AFM phases is in the band occupation [24]: The A-AFM phase is realized when the energy level of the Ru *xy* orbital is substantially lower than those of the *yz*, *zx* orbitals. Here we define *x*, *y* and *z* in the tetragonal notation. Thus, two of the four *d*-electrons derived from Ru fully occupy the *xy* band and the others are in the half-filled yz/zx bands. In other words, the A-AFM phase is realized in a *xy*-ferro orbital ordered state. The B-AFM phase starts to emerge when the energy difference between the *xy* and yz/zx orbitals

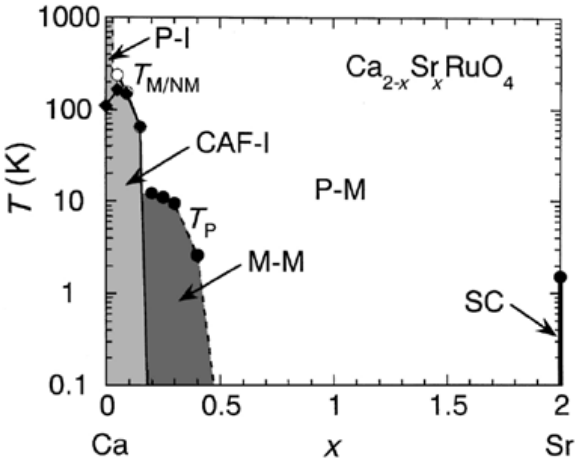

Figure 2.5: Sr-substitution dependence of the ground state of $Ca_{2-x}Sr_xRuO_4$ [11]. SC, P-M, M-M, CAF-I and P-I denote superconducting, paramagnetic metallic, metamagnetic metallic, canted antiferromagnetic insulating and paramagnetic insulating, respectively.

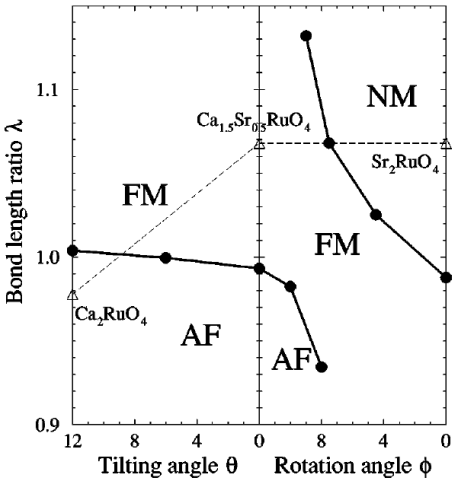

Figure 2.6: Magnetic phase diagram of $Ca_{2-x}Sr_xRuO_4$ based on first principle calculation [19].

decreases by partial release of the flattening: electrons in the *xy* band are transfered to the *yz*/*zx* band, leading to an antiferro orbital order with the B-AFM order. When the flattening distortion is completely released, *xy*, *yz* and *zx* orbitals are energetically degenerate and occupations of each orbital become 4/3, and then metallic phase is realized.

Under hydrostatic pressure, FM order [8, 7, 44, 45] and SC transition [9] are observed in addition to the Mott transition, as shown in Fig. 2.7 (a). The FM-M phase realizes between 0.5 and 8 GPa, and the maximum of the Curie temperature T_{FM} is 28 K at 7 GPa. Although the FM long-range order is realized under hydrostatic pressure, only development of FM fluctuation is observed by chemical substitution.

The SC phase emerges above 9 GPa and the SC transition temperature T_c is 0.4 K at 10 GPa.

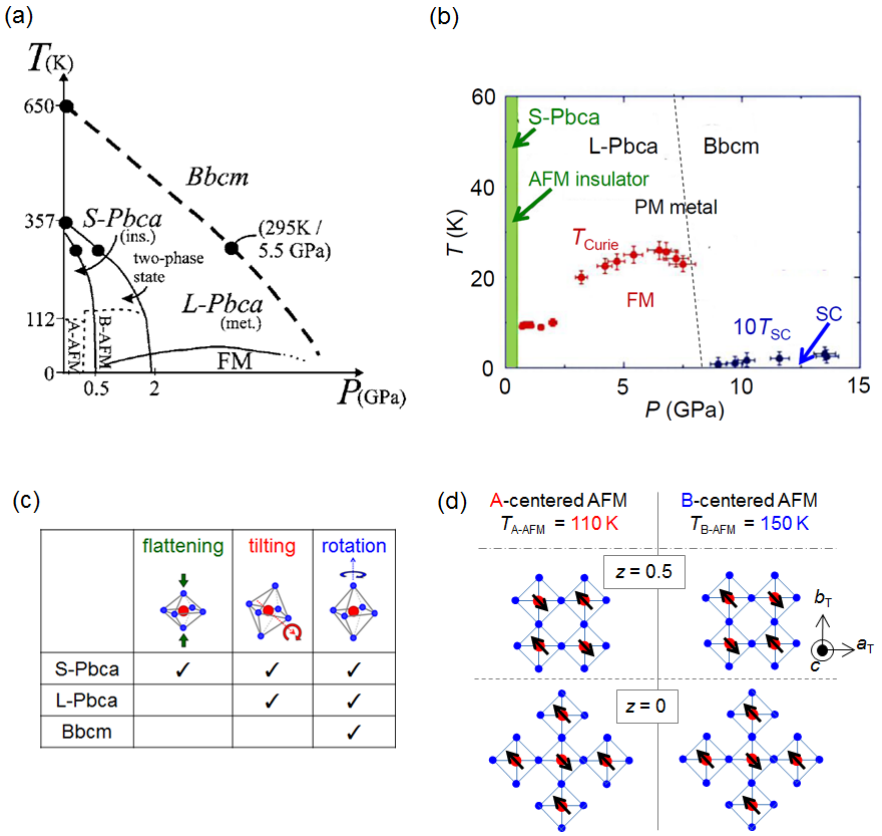

Figure 2.7: (a, b) Pressure-temperature phase diagram of Ca_2RuO_4 [6, 9]. The panel (a) captures higher temperature region, while the panel (b) features higher pressure region. (c) Correspondence between the name of crystal structure in the group-theory notation and the lattice distortion in the case of Ca_2RuO_4. This figure is made based on the results of Ref. [6]. (d) Spin configuration of Ca_2RuO_4 at the AFM orders. This figure is drawn based on Ref. [5].

Because the SC phase is located next to the FM phase and a chemical-substituted material Sr_2RuO_4 exhibits spin-triplet superconductivity, the hydrostatic-pressure-induced SC of Ca_2RuO_4 is also expected to be of spin-triplet. Thus, Ca_2RuO_4 will be a new object for studying spin-triplet superconductivity. However, the high critical pressure of 9 GPa makes it difficult to reveal detailed properties of the superconductivity of Ca_2RuO_4. Therefore, it is significantly important to search for possible superconductivity under UAP, which may induce superconductivity with a lower pressure than the hydrostatic pressure. Relation between crystal structure and ground state is not completely clarified for emergence of superconductivity in Ca_2RuO_4, differently from the case of Mott transition of Ca_2RuO_4. However, as far as considering known experimental results, it seems that the FM order disappears and the superconductivity emerges at around the pressure where the release of tilting distortion occurs, as shown in Figs. 2.7 (b) and 2.9). Therefore, we can predict that some external force to release both the flattening and tilting distortion of RuO_6 octahedra is preferable for inducing superconductivity in Ca_2RuO_4.

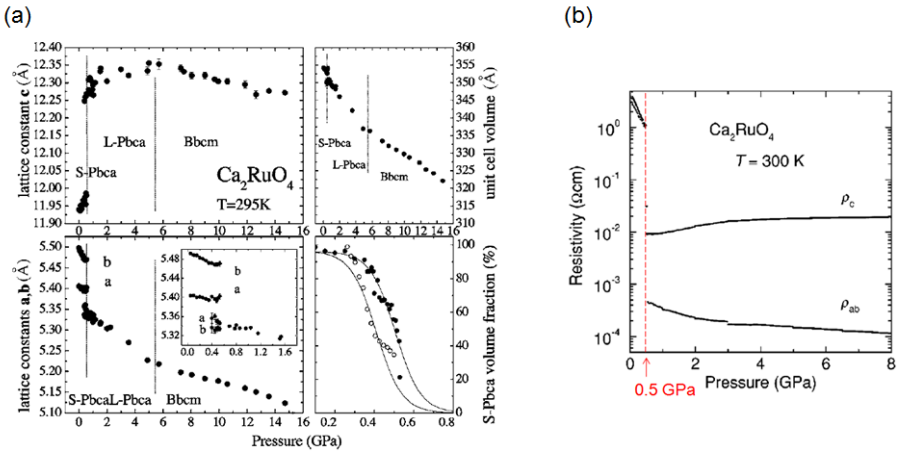

Figure 2.8: (a) Hydrostatic pressure dependence of lattice parameter of Ca_2RuO_4 [6]. (b) Hydrostatic pressure dependence of electric resistivity of Ca_2RuO_4 [8].

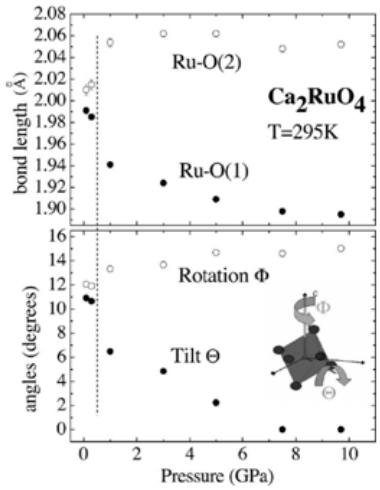

Figure 2.9: Hydrostatic pressure dependence of lattice distortion of Ca_2RuO_4 [6].

2.1.4 Temperature

With increasing temperature, flattening and tilting distortions are released at 357 K and 650 K, respectively, as shown in Figs. 2.7 (a) and 2.10 (a) [6, 2]. Above 357 K, where flatteing distortion is released, metallic state is realized as shown in Fig. 2.10 (b) [2]. With decreasing temperature, Ca_2RuO_4 exhibits antiferromagnetic order below 110 K as shown in Fig. 2.11 [2].

2.1.5 Electric field

Electric field above 40 V/cm [16] also makes Ca_2RuO_4 metallic by releasing the flattening distortion of RuO_6 octahedra, as shown in Fig. 2.12 [16].

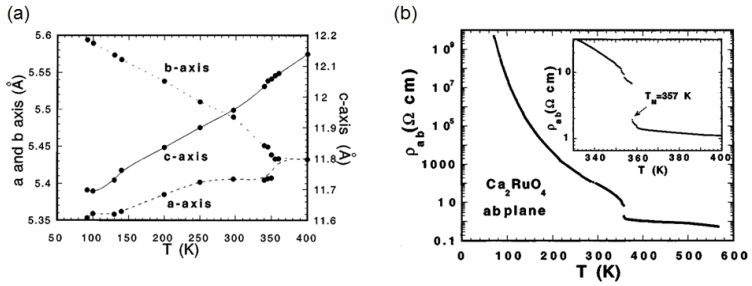

Figure 2.10: (a) Temperature dependence of the lattice parameter of Ca_2RuO_4 [2]. (b) Temperature dependence of the electric resistivity of Ca_2RuO_4 [2].

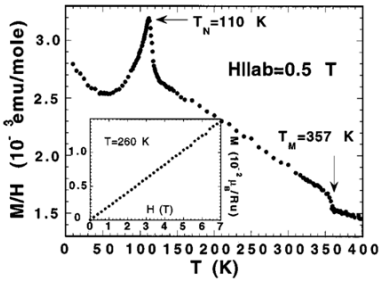

Figure 2.11: Temperature dependence of magnetization of Ca_2RuO_4 [2].

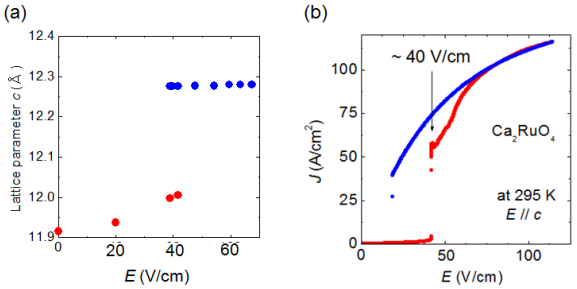

Figure 2.12: (a) Electric field dependence of lattice parameter of Ca_2RuO_4 [16]. (b) Electric field dependence of electric resistivity of Ca_2RuO_4 [16].

2.1.6 Thin film

FM-M behavior is also observed in Ca_2RuO_4 thin films as shown in Fig. 2.13, where in-plane epitaxial stress leads to a structural change (Fig. 2.1 (c)) [14, 15, 39].

2.2 Spin-triplet superconductor Sr_2RuO_4

In almost all superconductors including high-transition-temperature cuprates, electronic Cooper pairs are of spin-singlet. In contrast, atomic Cooper pairs of superfluid ^{3}He are of spin-triplet.

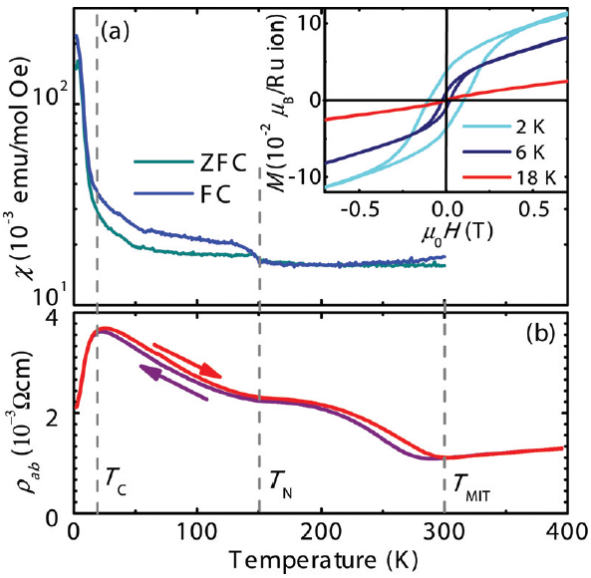

Figure 2.13: Ferromagnetic metallic behavior in Ca_2RuO_4 thin film [15].

Then whether spin-triplet superconductivity exists or not has been an intriguing question in the research field of superconductivity and many researchers studied to find the answer of this question. At present, the following materials are leading candidates for spin-triplet superconductors: Sr_2RuO_4, UPt_3, UBe_{13}, UNi_2Al_3, $PrOs_4Sb_{12}$, and ferromagnetic superconductors such as UGe_2, URhGe, UCoGe. Moreover, in superconductors whose crystal structures do not have the inversion symmetry, the possibility of the mixing state of spin-triplet and singlet Cooper pairs is theoretically proposed. Examples of non-centro-symmetric superconductors are $CePt_3Si$, $CeIrSi_3$, $CeRhSi_3$, $Li_2(Pt,Pd)_3B$, and UIr.

Among these candidates for spin-triplet superconductors, Sr_2RuO_4 has many evidences of spin-triplet superconductivity [46, 47, 48]. Moreover, the electronic structure of Sr_2RuO_4 is simple and all the Fermi surfaces are known [3]. Therefore, Sr_2RuO_4 is an ideal material for studying spin-triplet superconductivity.

2.2.1 Fundamental properties of Sr_2RuO_4

Sr_2RuO_4 has a layered perovskite crystal structure similar to the structure of high-transition-temperature cuprate superconductors $La_{2-x}Ba_xCuO_4$. The electric conductivity is governed by the RuO_2 layers. In the perovskite-based crystal structure, a transition-metal ion is octahedrally surrounded by oxygen ions. Then the degeneracy of the five d orbitals of the transition metal is partially removed due to the crystal-field effect, and the d levels split into two degenerate e_g orbitals ($x^2 - y^2$ and $3z^2 - r^2$) and three degenerate t_{2g} orbitals (xy, yz, zx). In case of the 4d orbitals, the energy splitting between the t_{2g} orbitals and the e_g orbitals is more important than Hund's coupling. Therefore, in Ru-based perovskites, four 4d electrons per one Ru ion choose low spin state and occupy the t_{2g} orbitals. In Sr_2RuO_4, the t_{2g} orbitals of Ru hybridize with the

p orbitals of O on RuO_2 layers and form bands. The band originating from the *xy* orbital is two dimensional and the band originating from the *yz* and *zx* orbital is one dimensional (Fig. 2.14). On the k_xk_y plane, the two-dimensional band forms a circular Fermi surface, while each one-dimensional band forms a straight Fermi surface. However, the actual Fermi surfaces originating from the *yz* and *zx* bands are rounded squares because of small hybridization of the *yz* and *zx* bands. As a result, three cylindrical Fermi surfaces are expected as shown in Fig. 2.15. Actually, such Fermi surfaces are observed in dHvA experiments(Fig. 2.16) [3]. The α surface is a hole Fermi surface originating from the *yz*-*zx* hybridization band, the β surface is an electronic Fermi surface originating from the *yz*-*zx* hybridization band, and the γ surface is an electronic Fermi surface originating from the *xy* band. The cylindrical shapes of these Fermi surfaces indicate that the electronic state of Sr_2RuO_4 is quasi two dimensional and support the expectation that the conduction occurs mainly in the RuO_2 plane. The effective electronic masses of the α, β, and γ surfaces are 3.4, 7.5, and 14.6 times as large as the mass of the free electron. These electronic masses suggest that electron-electron interaction is moderately strong in Sr_2RuO_4; non-Fermi liquid behavior has not been observed and the normal state can be quantatively described well as Fermi liquid.

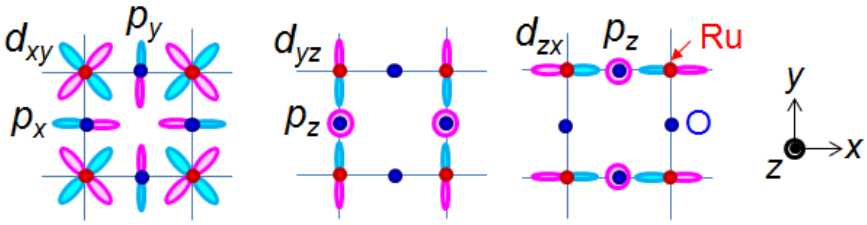

Figure 2.14: Hybridization between 4*d* orbital of Ru and 2*p* orbital of O.

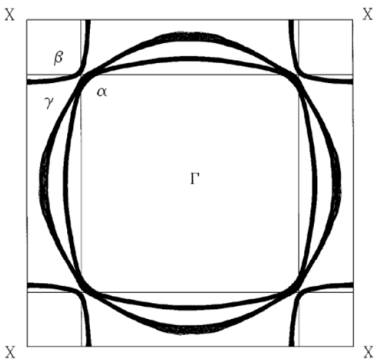

Figure 2.15: Fermi surfaces of Sr_2RuO_4 determined by band calculation [49].

Sr_2RuO_4 exhibits superconductivity below 1.5 K and the electronic Cooper pairs are believed to be of spin-triplet chiral *p* wave (S=1, L=1). The superconductivity is mainly driven by the γ surface. Just after the superconductivity was discovered, Sr_2RuO_4 attracted much interest as a reference material of high-transition-temperature cuprate superconductors. Later, how-

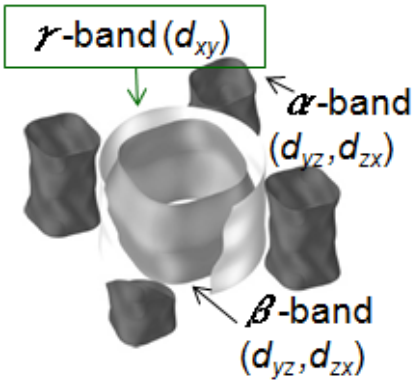

Figure 2.16: Fermi surfaces of Sr_2RuO_4 determined by dHvA experiment [3].

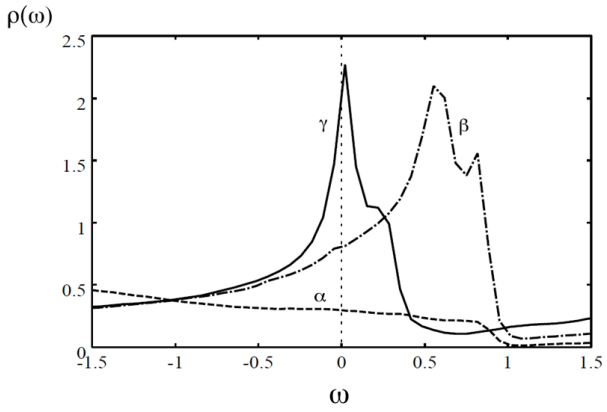

Figure 2.17: Density of states of the three bands in Sr_2RuO_4 [50].

ever, the possibility of spin-triplet superconductivity of Sr_2RuO_4 was pointed out [51], because $SrRuO_3$ and $Sr_4Ru_3O_{10}$ exhibits ferromagnetism [52] among Ruddlesden-Popper type ruthenates $Sr_{n+1}Ru_nO_{3n+1}$, to which Sr_2RuO_4 belongs, and the Fermi liquid parameters of Sr_2RuO_4 are similar to those of ^{3}He. Then several studies were performed for verifying the hypothesis. First, non *s*-wave superconductivity of Sr_2RuO_4 was clarified from the absence of coherence peak in nuclear magnetic relaxation rate $1/T_1$ [53] and from the significant suppression of T_c by nonmagnetic impurity (Fig. 2.18) [54] or by lattice defect [55]. Moreover, constant Knight Shift below T_c in nuclear magnetic resonance (NMR) measurements under field in the *ab* plane (Fig. 2.19) revealed that the superconductivity is a spin-triplet state (S=1, S_z=0) in which spins are perpendicular to the *c* axis [46, 47]. The same result was obtained in the polarized neutron scattering experiment [48].

Orbital part of the SC order parameter of Sr_2RuO_4 is considered to be a chiral state, in which time reversal symmetry is broken. The experimental results of muon spin relaxation (μSR) [56] and Kerr rotation [57] indicate that local internal magnetic field emerges below T_c and time reversal symmetry is spontaneously broken (Fig. 2.20). Based on this result and the fact that the spin part of the superconductivity of Sr_2RuO_4 is S_z=0 and does not have internal magnetic field, it is

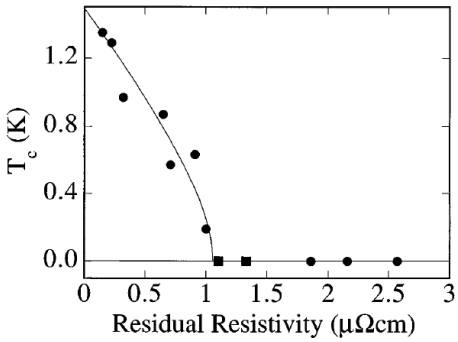

Figure 2.18: Suppression of T_c by nonmagnetic impurity in Sr_2RuO_4 [54].

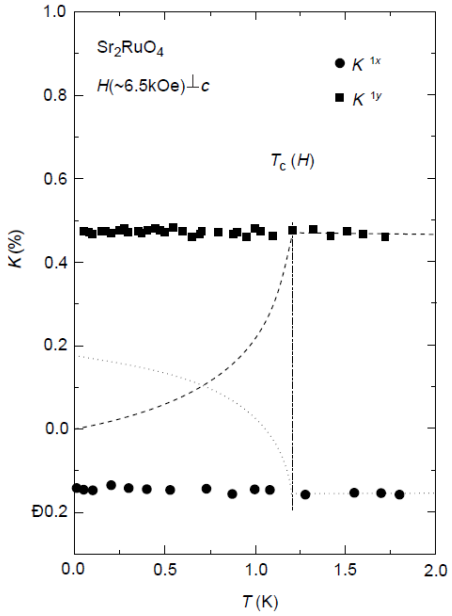

Figure 2.19: Knight Shift of Sr_2RuO_4 [46].

concluded that the observed internal magnetic field originates from the orbital part and the orbital part of the superconductivity of Sr_2RuO_4 is $L_z \pm 1$.

A strong candidate of the d vector describing the SC state of Sr_2RuO_4, in which the spin and orbital part is S_z=0 and $L_z \pm 1$, is

$$d = \Delta\hat{z}(k_x + ik_y) \, .$$

This d vector is isotropic in the k_xk_y plane reflecting the symmetry of the crystal structure and the states described by k_x and k_y are degenerate in the orbital part. It is theoretically predicted that the degeneracy of the states of k_x and k_y is resolved and double SC transition occurs when in-plane isotropy is broken by UAP or magnetic field [35, 36]. As described in Fig. 2.23, the phase whose SC order parameter consists of one component (k_x) is expected in a high-temperature region ($T_2 < T < T_1$), while the phase whose SC order parameter has two components ($\lambda_x(T)k_x + i\lambda_y(T)k_y$)

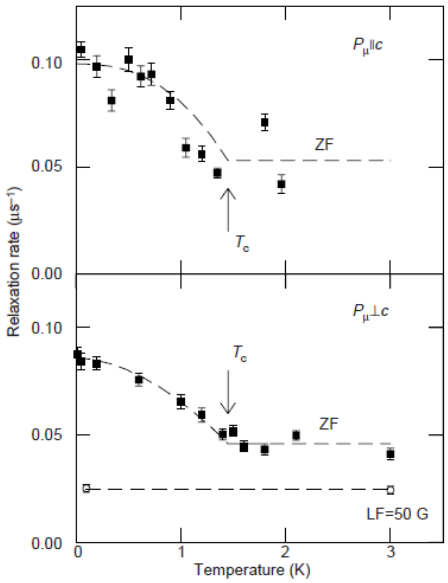

Figure 2.20: μSR experiment of Sr_2RuO_4 [56].

realizes in the lower temperature region ($0 < T < T_2$). If such a situation is really induced, imaginary part of AC magnetic susceptibility or specific heat is expected to exhibit two anomalies corresponding to the SC transitions at T_1 and T_2.

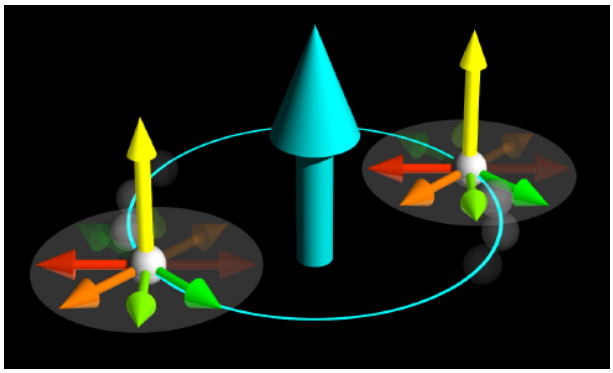

Figure 2.21: Strongest candidate for the *d* vector of Sr_2RuO_4.

Under magnetic field, SC double transition has already been reported in specific heat [58, 59] and AC magnetic susceptibility [60] (Fig. 2.24). However, these double transitions exist only in low-temperature and high-magnetic-field region, although double transition is theoretically expected to start just below T_c. Therefore, these double transitions observed in magnetic field can not be explained only by the assumption that SC order parameter in zero field is multi-component, and the origin of the phenomena is still unclear. Therefore, to clarify whether SC double transition occurs under UAP is essential for determining the SC order parameter of Sr_2RuO_4. In other words, if double transition is observed under in-plane UAP, it would be a crucial proof that the SC order

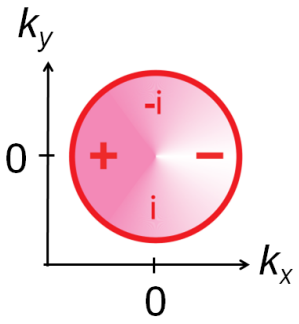

Figure 2.22: Orbital part of the SC order parameter of Sr_2RuO_4.

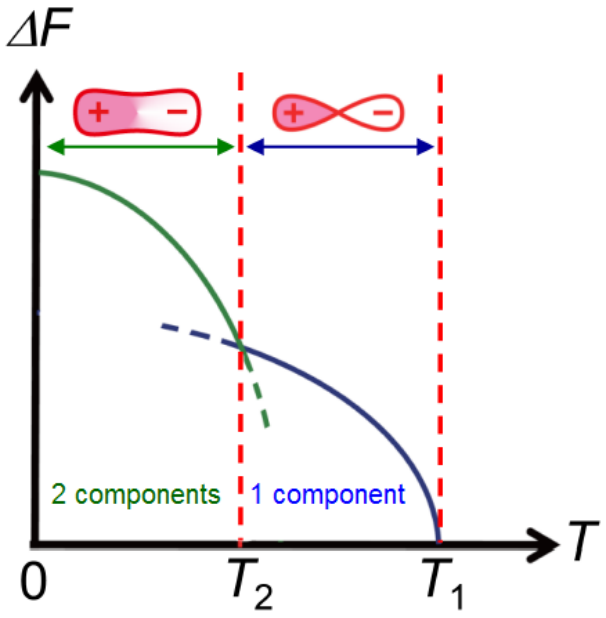

Figure 2.23: Expected SC double transition in Sr_2RuO_4.

parameter of Sr_2RuO_4 is multi-component.

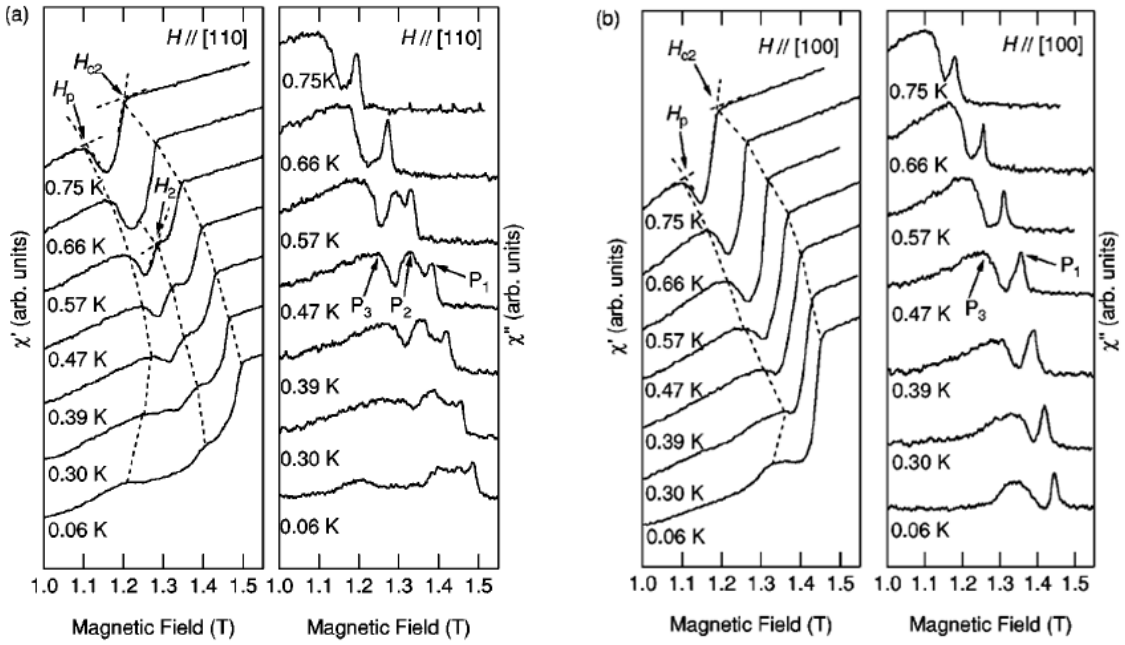

Figure 2.24: Double transition of AC magnetic susceptibility of Sr_2RuO_4 [60].

2.2.2 Sr_2RuO_4-Ru eutectic crystal

The Sr_2RuO_4-Ru eutectic crystal discovered during the process to improve the quality of the single crystal of Sr_2RuO_4 is also interesting. In order to synthesize Sr_2RuO_4 [61], firstly, mixture of $SrCO_3$ and RuO_2 is calcined and polycrystal of $Sr_2Ru_nO_{2n+2}$ is obtained:

$$2SrCO_3 + nRuO_2 \rightarrow Sr_2Ru_nO_{2n+2} + 2CO_2 \ . \tag{2.1}$$

Then a single crystal is grown by the floating zone method. What should be noted is that Ru evaporates as RuO_2 in this process:

$$Sr_2Ru_nO_{2n+2} \rightarrow Sr_2Ru_{n'}O_{2n'+2} + (n - n')RuO_2 \tag{2.2}$$

Therefore, in order to get Sr_2RuO_4 single crystal without Ru deficiency, the initial n should be larger than 1 and the synthesis is usually performed with $n = 1.15$. If the proportion of RuO_2 increases more and n becomes 1.2, Ru metal originating from the excess Ru is embedded in Sr_2RuO_4 single crystal. As shown in Fig. 2.25, Ru pieces appears quasi periodically. The typical dimensions of the Ru pieces are 1 μm $\times$ 10 μm $\times$ 30 μm and the typical distance between Ru pieces is 10 μm. The black and white part in Fig. 2.25 are Sr_2RuO_4 and Ru pieces, respectively. Figure 2.26 represents the cross section of cylindrical single crystal, and the inner and outer part tends to become Sr_2RuO_4-Ru eutectic and pure Sr_2RuO_4, respectively. Since Ru evaporation is suppressed, Sr_2RuO_4-Ru eutectic is obtained inside.

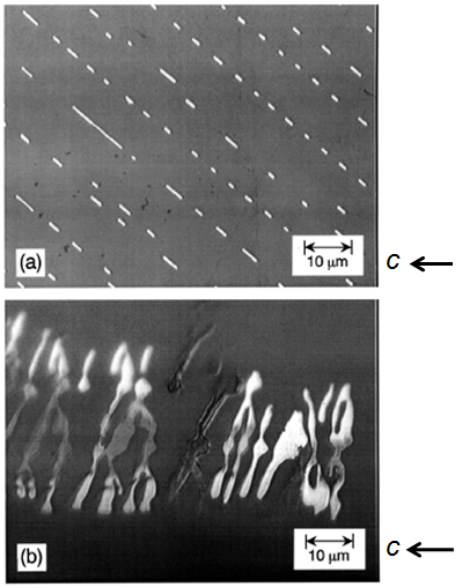

Figure 2.25: Picture of Sr_2RuO_4 under a polarizing microscope [29].

Sr_2RuO_4-Ru eutectic is curious because of the enhancement of T_c. Although T_c of Sr_2RuO_4 and Ru is 1.5 K and 0.49 K, respectively, the onset T_c of Sr_2RuO_4-Ru is enhanced up to 3 K. This eutectic is thus called as the "3-K phase" after the onset SC temperature. Although the mechanism of the T_c enhancement in the eutectic crystal is not fully clarified, several properties of the eutectic are revealed as follows:

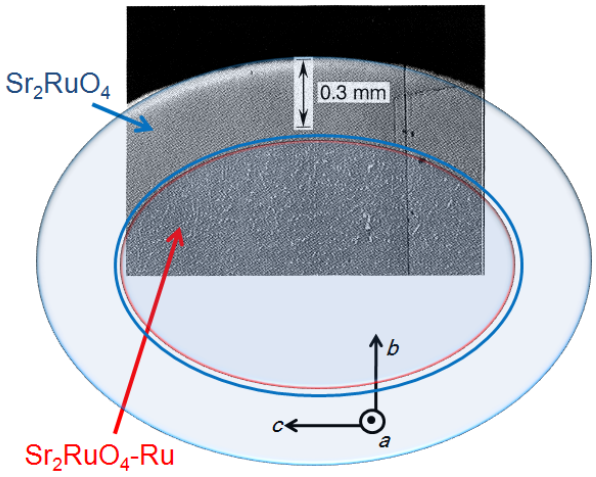

Figure 2.26: Picture of Sr_2RuO_4-Ru eutectic under a polarizing microscope [30].

1. AC magnetic susceptibility and electric resistivity of Sr_2RuO_4-Ru (Fig. 2.27) exhibit broad SC transition from 3 K to 1.5 K [29]. Moreover, the SC transition of pure Ru at 0.49 K is also observed in AC susceptibility measurements. These results suggest that in Sr_2RuO_4-Ru some part becomes SC at 3 K, SC region expands on cooling, the whole part of Sr_2RuO_4 exhibits superconductivity at 1.5 K, and the whole system becomes SC at 0.49 K.

2. Absence of anomaly around 3 K in specific heat (Fig. 2.28) suggests that superconductivity at 3 K is non-bulk [62]. This result indicates that interface between Sr_2RuO_4 and Ru becomes SC at 3 K and the SC region expands on cooling because of the proximity effect.

3. The 3-K superconductivity in Sr_2RuO_4-Ru eutectic exhibits anisotropy which is similar to the anisotropy of the superconductivity in Sr_2RuO_4: both superconductivity is strong against the field in the *ab* plane but weak against the field along the *c* axis (Fig. 2.29) [30]. The zero bias conductance peak (ZBCP), which occurs only in non *s*-wave superconductors, is observed above 1.5 K in the eutectic. This result indicates that the superconductivity above 1.5 K in the eutectic is *p*-wave, being similar to the superconductivity in Sr_2RuO_4(Fig. 2.30) [63, 64]. Moreover, it has recently been revealed that proximity effect of the 3-K phase superconductivity does not penetrate into the Ru metal region [65]. These results suggest that the 3-K superconductivity in the eutectic occurs only in the Sr_2RuO_4 side of the interface.

4. Sigrist *et al*. proposed phenomenological theory concerned with temperature dependence of SC order parameter in the eutectic based on the description that the Sr_2RuO_4 region around interfaces between Sr_2RuO_4 and Ru exhibits *p*-wave superconductivity at 3 K [66]. Around the interface, spatial symmetry is reduced because of the existence of a Ru inclusion. Thus, the degeneracy of k_x and k_y states is resolved, and the SC state whose wave function elongates along the interface (it corresponds to k_x in Fig. 2.31) has higher T_c. Therefore, the superconductivity with one-component orbital order parameter emerges at

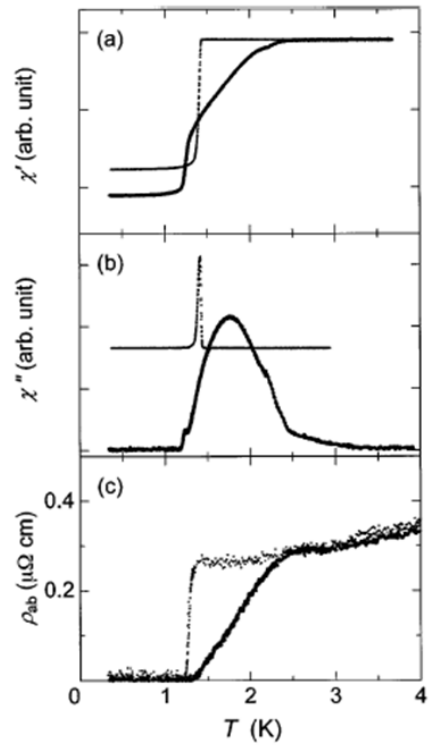

Figure 2.27: AC magnetic susceptibility and electric resistivity of Sr_2RuO_4-Ru [29].

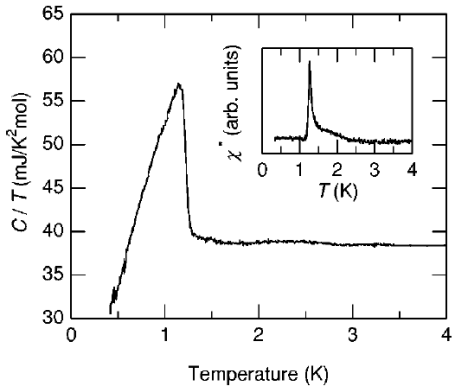

Figure 2.28: Specific heat of Sr_2RuO_4-Ru [62].

3 K. With decreasing temperature, the two-component superconductivity (it corresponds to k_y in Fig. 2.31) is realized.

5. The theory mentioned above describes also the phenomenon in Sr_2RuO_4-Ru that the SC onset temperature is different from the temperature at which ZBCP appears (Fig. 2.32). The ZBCP appears as a consequence of formation of Andreev bound states, which is realized

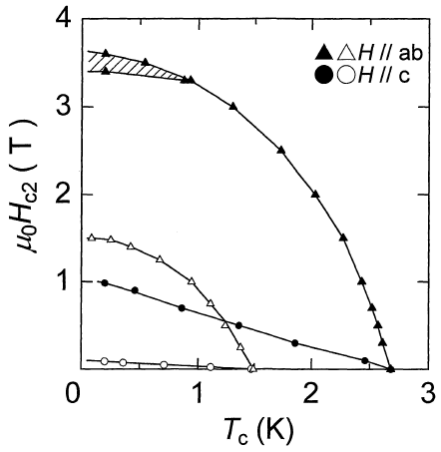

Figure 2.29: Anisotropy of the upper critical magnetic field of Sr_2RuO_4-Ru eutectic [30].

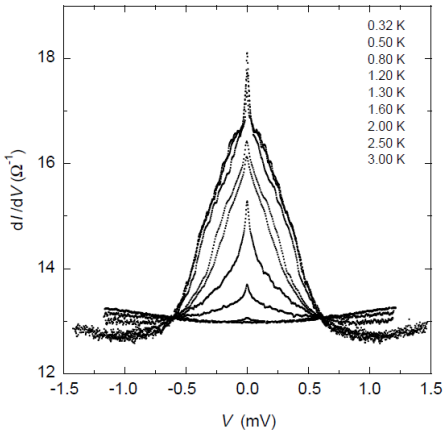

Figure 2.30: Zero bias conductance peak of Sr_2RuO_4-Ru eutectic [63].

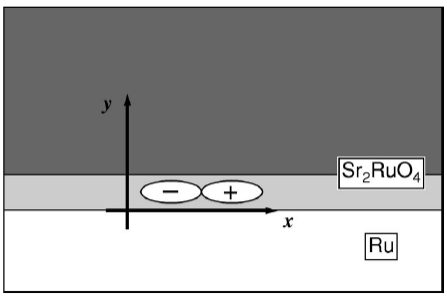

Figure 2.31: SC order parameter of Sr_2RuO_4-Ru eutectic at 3 K [62].

when the phase difference between the pair potential for incident electronic quasi-particles and that for reflective hole quasi-particles is π. Thus order parameter component elongating

perpendicular to the interface (k_y in Fig. 2.31) is required for ZBCP. Therefore, ZBCP appears at temperature lower than the onset T_c.

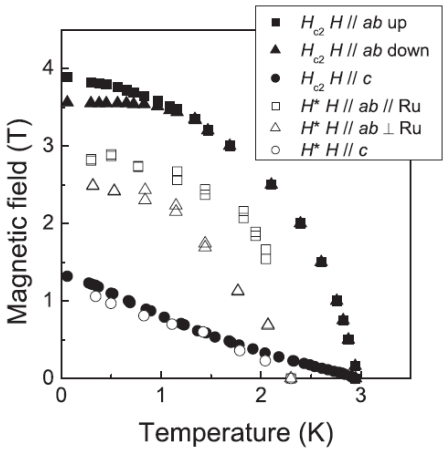

Figure 2.32: Comparison between upper critical magnetic field and the magnetic field of ZBCP appearance in Sr_2RuO_4-Ru eutectic [64].

Summarizing the above, the strong candidate for describing the superconductivity in Sr_2RuO_4-Ru eutectic is that the Sr_2RuO_4 region around the interface between Sr_2RuO_4 and Ru exhibits superconductivity at 3 K and the SC region expands only into Sr_2RuO_4 side by proximity effect (Fig. 2.33). Because there must be an anisotropic lattice distortion at the interface due to a lattice mismatch between Sr_2RuO_4 and Ru, one possible origin of the T_c enhancement is anisotropic lattice distortion. Therefore, investigation of the UAP effect on T_c should provide a crucial hint to solve the mechanism of the T_c enhancement in Sr_2RuO_4-Ru eutectic.

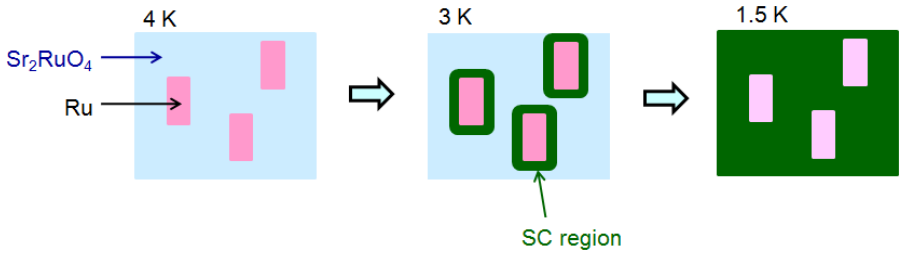

Figure 2.33: Interfacial superconductivity in Sr_2RuO_4-Ru eutectic

2.2.3 Pressure effect on Sr_2RuO_4

It had already been revealed experimentally that T_c of Sr_2RuO_4 is suppressed by hydrostatic pressure and the pressure dependence of T_c is $dT_c/dP_{hydro} = -0.2$ K/GPa (Fig. 2.34) [33, 34].

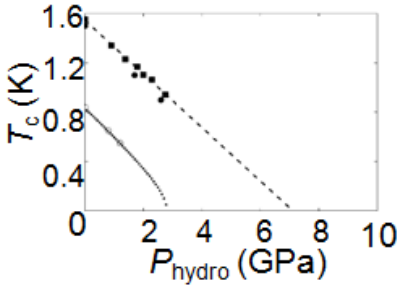

Figure 2.34: Hydrostatic pressure dependence of the SC transition temperature of Sr_2RuO_4 [34].

Before our UAP studies on Sr_2RuO_4 UAP effects on T_c were predicted based on band calculation [50] and elastic approximation [67]. In both cases, T_c was expected to decrease for $P_{\|a}$ and increase for $P_{\|c}$. The prediction from the band calculation is based on changes of the density of states (DOS) by UAP. The γ band, which is considered to be responsible for the superconductivity, should shift by UAP relative to the other bands due to the crystalline field effect. Then the DOS at Fermi level $D(\epsilon_F)$ of the γ band changes accordingly and $T_c \sim \exp(-1/\lambda D)$ should be also affected. As shown in Fig. 2.35, under UAP along the a axis, the enegy of the xy orbital, which is the origin of the γ band, is enhanced. In other words, the γ band shifts to high energy side. Then $D(\epsilon_F)$ of the γ band is suppressed and T_c is expected to decrease. In contrast, under UAP along

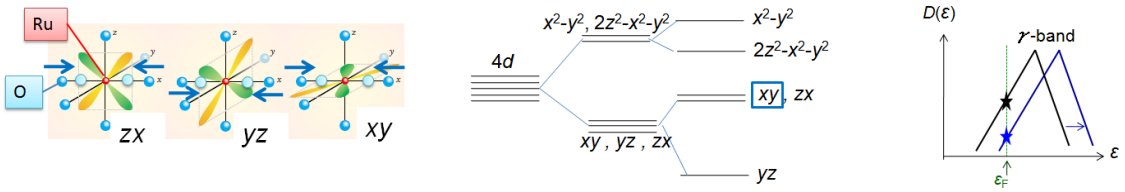

Figure 2.35: Prediction of the a-axis UAP effect on Sr_2RuO_4

the c axis, since $D(\epsilon_F)$ of the γ band is enhanced as shown in Fig. 2.36, T_c is expected to increase.

The prediction from an elastic approximation, is made based on the Ehrenfest relation and the results of the ultrasonic experiments. First, $\frac{dT_c}{d\epsilon_i}$ is obtained by putting the values of $\Delta C_{ii}(T_c)$ estimated from the result of ultrasonic experiment (Fig. 2.37) [67] to the Ehrenfest equation

$$\left(\frac{dT_c}{d\epsilon_i}\right)^2 = -\frac{V_{mol} T_c \Delta C_{ii}(T_c)}{\Delta c_p(T_c)} \qquad (i = 1, 3) \tag{2.3}$$

(ϵ: longitudinal strain, V_{mol}: volume per 1 mol, C_{ii}: longitudinal modulus, c_p: specific heat, i=1 and 3 correspond to the a and c axis, respectively.).

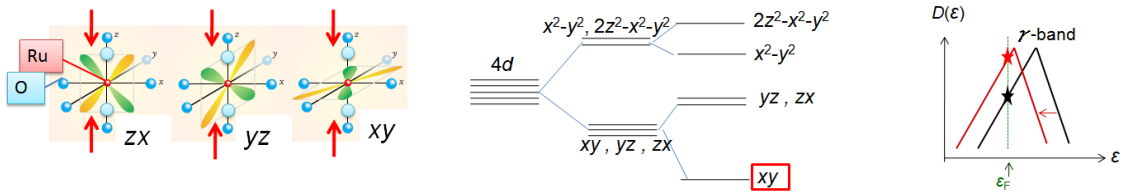

Figure 2.36: Prediction of the *c*-axis UAP effect on Sr_2RuO_4

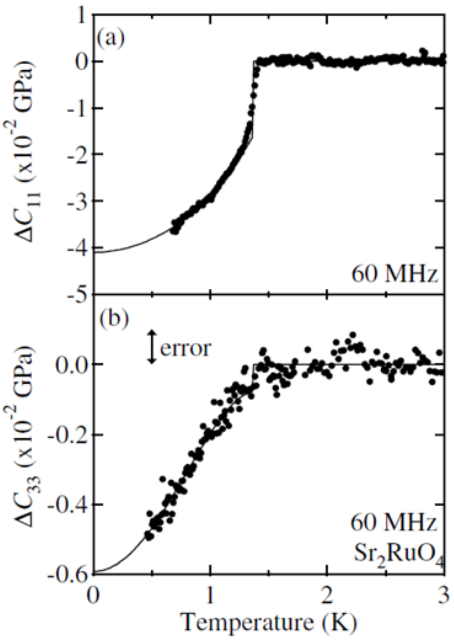

Figure 2.37: Elastic modulus of Sr_2RuO_4 estimated by ultrasonic experiment [67].

Then, by solving the following equations about i=1 and 3,

$$\frac{dT_c}{d\epsilon_i} = -\sum_j C_{ij}\frac{dT_c}{dP_j} \qquad (i = 1,3, \quad j = 1,2,3)\,, \tag{2.4}$$

$dT_c/dP_1(= dT_c/dP_a)$ and $dT_c/dP_3(= dT_c/dP_c)$ are obtained. Since $\frac{dT_c}{d\epsilon_i}$ have two possible answers (plus and minus), there are four possibilities for the combination of dT_c/dP_1 and dT_c/dP_3 as the answer of Eq. 2.4. If hydrostatic pressure effect is considered to be a linear combination of the UAP effects along the *a*, *b* and *c* axis,

$$\frac{dT_c}{dP_{\rm hydro}} = 2\frac{dT_c}{dP_a} + \frac{dT_c}{dP_c} \tag{2.5}$$

at least one of dT_c/dP_a or dT_c/dP_c should be minus because $dT_c/dP_{\rm hydro}$ is minus. To satisfy this condition, dT_c/dP_a and dT_c/dP_c are chosen to be -1.3 K/GPa and $+1$ K/GPa, respectively.

The experimental study of UAP effect on the superconductivity of Sr_2RuO_4-Ru eutectic was reported in 2009 [68, 69]. The temperature dependence of the DC magnetization above 1.8 K (Fig. 2.38) revealed that magnetic shielding fraction below onset T_c is enhanced with increasing pressure under any of the UAPs along the *c* axis, the *a* axis and the [110] direction although onset T_c is not changed by the pressures. Moreover, the rate of the enhancement of shielding fraction is larger under in-plane UAP than the *c*-axis UAP.

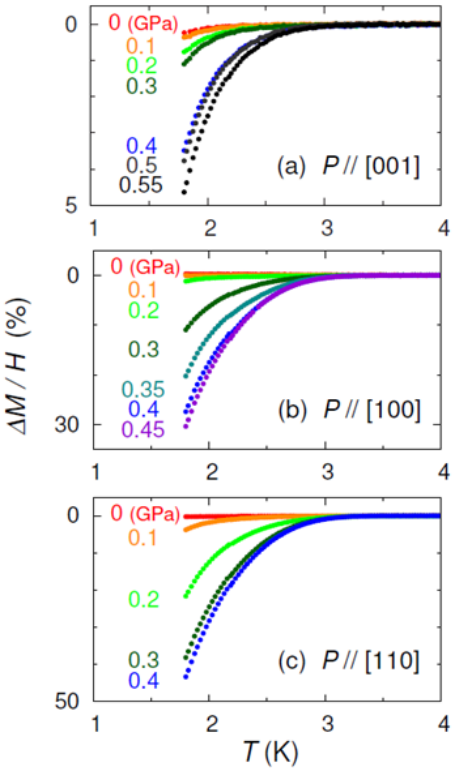

Figure 2.38: Temperature dependence of the DC magnetization of Sr_2RuO_4-Ru eutectic under UAPs [68].

In 2010, we reported the out-of-plane UAP effect on Sr_2RuO_4 [32]. We clarified that T_c of "pure" Sr_2RuO_4 is enhanced up to 3.2 K under pressure along the *c* axis ($P_{\|c}$). Here, "pure" means that the sample contains almost no Ru inclusions. The result strongly supports our scenario that the anisotropic lattice distortion plays an important role in the T_c enhancement. Moreover, in Sr_2RuO_4-Ru under $P_{\|c}$, we found a crossover at $P^*_{\|c} \sim 0.4$ GPa from behavior attributable to interfacial SC to behavior similar to that in pure Sr_2RuO_4 under $P_{\|c}$ [32].

Chapter 3

Development of uniaxial-pressure experimental technique

First of all, we constructed the system for UAP experiments.

3.1 Pressure apparatus

3.1.1 Pressure cell

To apply uniaxial pressure, we used piston-cylinder type pressure cells illustrated in Fig. 3.1. We used two designs of the pressure cell (the longer and shorter ones) depending on the purpose. As the common features of these pressure cells, a sample is pressed directly by the pistons without any pressure medium and the disc-shaped springs keep pressure by the tightened lock bolts. Based on our designs, the pressure cells were made by R&D Support.

The longer pressure cell (Fig. 3.1(a)) is designed mainly for magnetization measurement. Thus, the geometry is symmetric. All the inner parts are made of Be-Cu (hard alloy), whereas the outer body is made of polybenzimidazole (hard plastic) to reduce background contributions. Because the outer body is made of an electric insulator, this cell can be used also for two-wire resistivity measurement as described in detail in Chap. 3.2.1. The diameter of the pistons is 3 mm.

The shorter cell (Fig. 3.1(b)) was designed by myself for resistivity and AC susceptibility measurements. The most parts are made of Be-Cu. Depending on purposes, we chose Be-Cu or mixture of ZrO_2 and Al_2O_3 (insulator) for pistons, and polybenzimidazole or Be-Cu for the outer body. Although the diameter of the pistons is 4 mm, the sample diameter should be less than 3 mm because of the taper of the pistons. The improved points compared with the longer cell are the windows which enable accesses to the sample space from outside of the cell, the thin rod which penetrates the piston backup through windows and prevent the parts below the piston backup from rotating to break a sample, and the shorter length which enables the attachment to many refrigerators. Thanks to the windows, resistivity measurement, mini-coil susceptibility measurement, pressure calibration using a strain gauge, and direct thermal link between a sample and the bath are achived as described in detail in Chap. 3.1.3, 3.2.

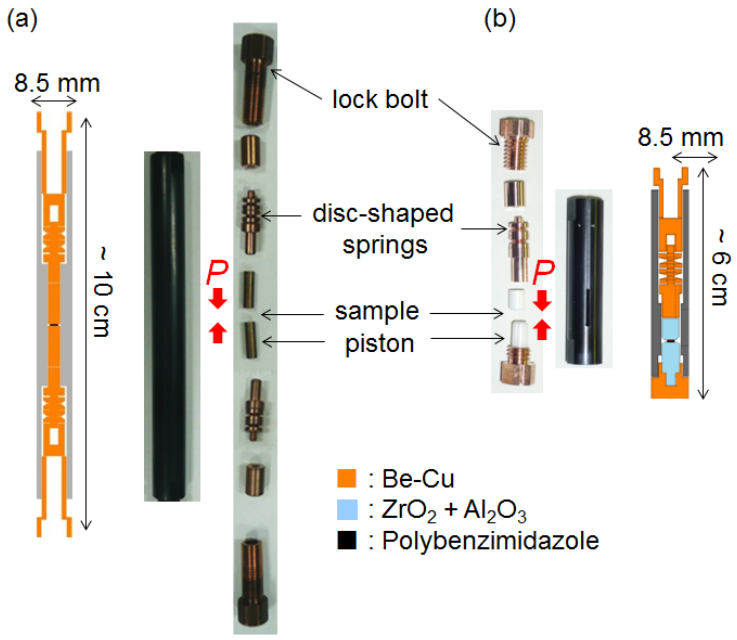

Figure 3.1: Photos and schematic figures of the uniaxial pressure cells used in this study. (a) Cell for magnetization and 2-wire resistivity measurement. Left figure is a schematic image of the cross section of the cell. Middle and right figure is the photo of the outer body and the inner parts, respectively. In the right photo, from top to bottom, a lock bolt, spring backup, disc-shaped springs, a piston backup, piston, piston, piston backup, disc-shaped springs, a spring backup, and lock bolt are represented. A sample is located between the pistons and pressed directly by the pistons as the pressure direction is shown by red arrows. (b) Cell for resistivity and AC susceptibility measurement. Left and middle figure is the photo of the inner parts and the outer body, respectively. Right figure is a schematic image of the cross section of the cell. In the left photo, from top to bottom, a lock bolt, spring backup, disc-shaped springs, a piston backup, piston, piston, and lock bolt are represented.

3.1.2 Pressurization

Pressure was applied to a sample at room temperature using the pressurize machine (PM) shown in Fig. 3.2(a). We have two PMs: the first PM (WG-KY01-4) was designed and made by Kyowa Seisakusho and used for the longer pressure cell, whereas I modified the design of the second PM for the use of the shorter pressure cell and asked HMD for its fabrication. As the common features of these PMs, they have two push rods inside: the bottom rod can be moved up and down by rotating the dial and change the force applied by PM (F_{PM}), whereas the top rod is fixed on the lid and connected to a load cell which gauges the value of F_{PM}.

As also illustrated in Fig. 3.2(b) the process of the pressurization is as follows: (1) Set a pressure cell in a PM and increase F_{PM} to an intended value by rotating the dial, (2) tighten the lock bolt of the cell, and (3) release F_{PM} completely by rotating the dial and take the cell out. At the end of the process (1) (in other words, at the state (B) of Fig. 3.2(b)), the force applied to a sample (F_{S}) is as same as F_{PM}, because the lock bolt of the pressure cell is loose and the force

applied by the lock bolt (F_{LB}) is zero. In the process (2), although the distance bewteen push rods of the PM does not change, F_{PM} is reduced because some force is covered by the lock bolt. At the end of the process (2) (in other words, at the state (C)), F_S becomes the sum of F_{PM} and F_{LB} and above the intended value. At the end of the process (3) (in other words, at the state (D)), F_S is as same as F_{LB}. In order to confirm that F_S is as same as the intended value, we performed the force calibrations as mentioned in Chap. 3.1.3.

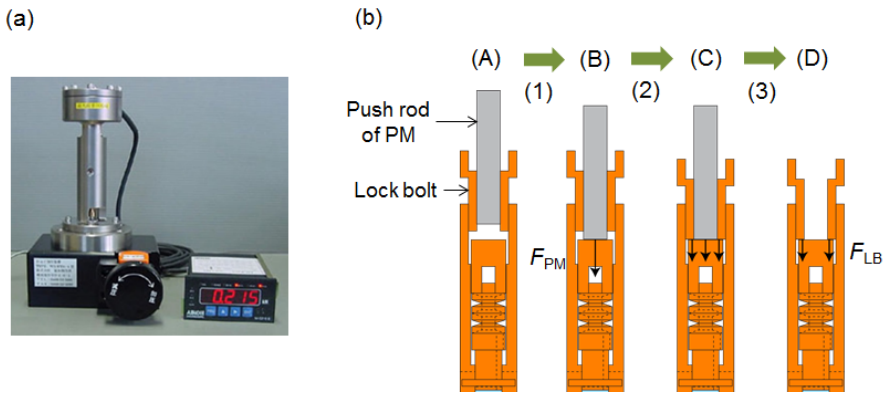

Figure 3.2: (a) Photo of the pressurize machine. (b) Schematic figure of the pressurization process. The states (A), (B), (C) and (D) and the processes (1), (2) and (3) correspond to the notation in the text and Fig. 3.3(b). F_{PM} and F_{LB} are the force applied by the pressurize machine and the lock bolt of the pressure cell, respectively.

3.1.3 Pressure estimation

Since samples are made to have cuboid shape, we estimated pressure value by dividing force by the sample area perpendicular to the force. The force value in the longer pressure cell was calibrated using superconducting transition of Pb and Sn as mentioned in Ref. [70]. The force value in the shorter cell was monitored using a strain gauge (KFRS-02-120-C1-13, Kyowa Dengyo), which was attached on a disc-shaped spring as shown in Fig. 3.3(a). The wires of the strain gauge are taken out through the hole of the piston backup and the window of the outer body.

The strain gauge on the spring changes its resistance R_{SG} depending on F_S, and F_{PM} can be read by the load cell. At the state (B) in Figs. 3.2(b) and 3.3(b), F_S is as same as F_{PM}, which is known to be an intended value. Therefore, in order to make F_S the intended value at the end of the pressurization process (in other words, at the state (D)), the lock bolt of the pressure cell should be tightened so that R_{SG} exhibit the same value between the state (B) and (D), as shown in Fig. 3.3(b).

R_{SG} was measured using the four-wire resistivity measurement mode of a Multimeter 2000 (Keithley).

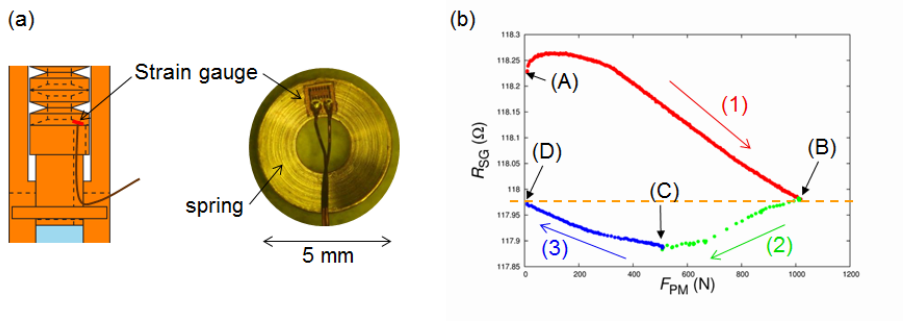

Figure 3.3: (a) Schematic figure and photo of the setting of the strain gauge for monitoring the force applied to a sample. (b) Changes during the pressurization process of the resistance of the strain gauge R_{SG} and the force applied by the pressurize machine F_{PM}. The states (A), (B), (C) and (D) and the processes (1), (2) and (3) correspond to the notation in the text and Fig. 3.2(b).

3.1.4 Sample preparation

Single crystals of Sr_2RuO_4 and Ca_2RuO_4 were grown by a floating-zone method [61, 1]. Sr_2RuO_4 crystals were synthesized in our Prof. Y. Maeno's Lab. and Ca_2RuO_4 crystals were provided by Prof. F. Nakamura. The directions of crystal axes were determined by the Laue method using a Back Reflection Laue Camera RASCO-BL 2 (Rigaku). Following the Laue information, samples were cut out by a Refine Saw RCA-005 (Refine Tec. Ltd.) to have a cuboid shape whose top and bottom surfaces are perpendicular to the direction along which pressure will be applied. Typical dimensions of samples for out-of-plane UAP are 0.5 mm along the pressure direction, and 2.0×2.0 mm^2 in the plane perpendicular to the pressure direction. In the case of samples for in-plane UAP, the plane perpendicular to the pressure direction has smaller area, because Ca_2RuO_4 and Sr_2RuO_4 cleave easily along the *ab* plane. Therefore, typical dimensions of samples for in-plane UAP are 0.5 mm along the pressure direction, and 2.0×0.5 mm^2 in the plane perpendicular to the pressure direction. Laue pictures were taken again after the cutting to check the misalignment (usually less than 10 degrees), and the top and bottom surfaces of the sample were polished with a tilt for modifying the alignment. The polishing has another purpose to make the two surfaces parallel to each other for improving pressure homogeneity. Polishing was performed with a Polishing Machine MA-200 (Musashino Denshi) with diamond slurries MP-9000(W), MP-1000(W) and MP-250(W) (Musashino Denshi). The side surfaces of a sample were covered with epoxy (Stycast 1266, Emerson-Cuming) to prevent the sample from breaking. In order to allow the epoxy to spread freely under pressure, enough space was kept between the epoxy and the inner wall of the pressure cell. Thanks to the space in addition to the result of a previous study which suggests that compressive force applied to oxides by surrounding Stycast 1266 is ignorable [71], uniaxial *pressure* not uniaxial *strain* is expected.

3.2 Measurements

3.2.1 Resistivity

Depending on a purpose, we performed two kinds of electric resistivity measurements: two-wire and four-wire methods. Although the resistance R measured by the two-wire method includes some extrinsic contributions, this two-wire method is easier than the four-wire method and still useful to detect the intrinsic change of the sample resistivity if the change is large.

Two-wire resistivity

For two-wire resistivity measurements, the longer pressure cell was used. By making use of the fact that the outer body is made of insulating plastic, we utilized the pistons made of Be-Cu metal as electrodes (Fig. 3.4(a)). In this method, electric current is applied parallel to the UAP direction. It should be noted that the measured resistance includes not only the sample resistance but also extrinsic resistance such as contact resistance between the sample and the piston or between the inner parts of the pressure cell and resistance of the inner parts themselves. However, this method has an advantage that measurement is easier than the four-wire method described in Chap. 3.2.1. In order to check the magnitude and the temperature dependence of the extrinsic resistance, we performed two-fire resistivity measurement using Au as a dummy sample (Fig. 3.4(b)). As a result, we have confirmed that the extrinsic resistance exhibits metallic behavior and is so small ($\sim 0.3\ \Omega$) that the metal-insulator transition is expected to be detected in this two-wire method. It should be noted that contact resistance cannot be measured in this two-wire method.

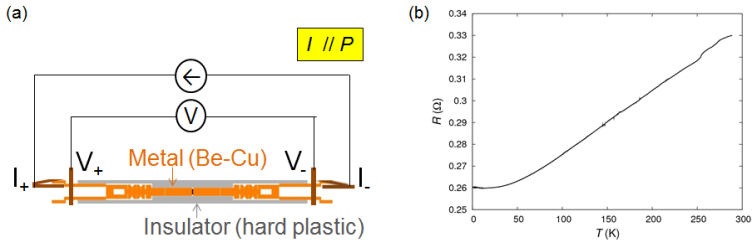

Figure 3.4: (a) Schematic figure of the setting of two-wire resistivity measurement. (b) Temperature dependence of the background resistance in this two-wire method. Au is used as a dummy sample.

At room temperature, resistance was measured while sweeping pressure with a DC current, whose direction was reverted in order to cancel the thermoelectric voltage. A DC current source 7651 (Yokogawa) and a Multimeter 2000 (Keithley) are utilized.

For measuring temperature dependence of resistance, we adopted an AC method using a Lock-in-amplifier SR830 (Stanford Research Systems) and ^{3}He cryostat Heliox VL (Oxford Instruments). In order to keep the amplitude of the electric current constant under the change of sample resistance, a resistance whose value is 10^3 times more than sample resistance is inserted in the circuit. The setting of the low temperature measurement is described in (Fig. 3.5). RuO_2 thermometers were attached at the top of the ^{3}He pot of the ^{3}He cryostat and the bottom of the

pressure cell. We confirmed that the difference between these temperatures is less than 10 mK in the lowest temperature range (~ 0.3 K). Since the top of the pressure cell which is the minus side of the electric circuit was electrically connected to the ^{3}He pot, the thermal link made of Au-plated Cu plate between the ^{3}He pot and the bottom of the cell which is the plus side of the circuit was electrically disconnected from the ^{3}He pot.

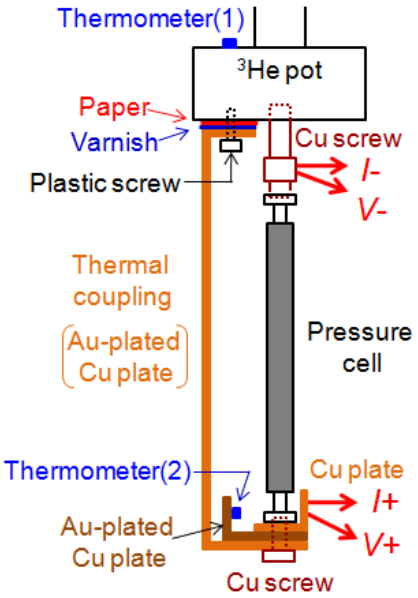

Figure 3.5: Schematic figure of the setting of two-wire resistivity measurement at low temperature.

Four-wire resistivity

For four-wire resistivity measurement, the shorter pressure cell was used. In this method, since the sample and electrodes directly touch the pistons, pistons made of mixture of ZrO_2 and Al_2O_3 were chosen for electrical insulation, whereas Be-Cu is selected for the material of the other parts. We adopted this four-wire method in the study of in-plane UAP effect on Ca_2RuO_4.The side surface of Ca_2RuO_4 sample was covered with epoxy to prevent cleaving, wires were put on the top surface of the sample (Fig. 3.6(a)). In order to improve pressure homogeneity, the wires should be as thin along the pressure direction as possible. Therefore, Au wires of diameter of 25 μm pressed to have thickness of 7 μm were just put without any conducting paste. In order to achieve good electric contact, Au was sputtered on the areas on which wires were put. Heat and electric field should be avoided during sputtering of Au on Ca_2RuO_4 because Ca_2RuO_4 crystals break down at the structural transition induced by heat (84 °C) or by electric field, For this purpose, a sample was put on a Cu plate as a heat sink and 5-min sputtering was performed 5 times with inserting 5-min intervals for cooling. The thickness of the sputtered Au is about 120 nm. In this four-wire resistivity measurement, current is applied perpendicular to the UAP direction.

Both in the pressure sweep at room temperature and in the temperature sweep at a fixed

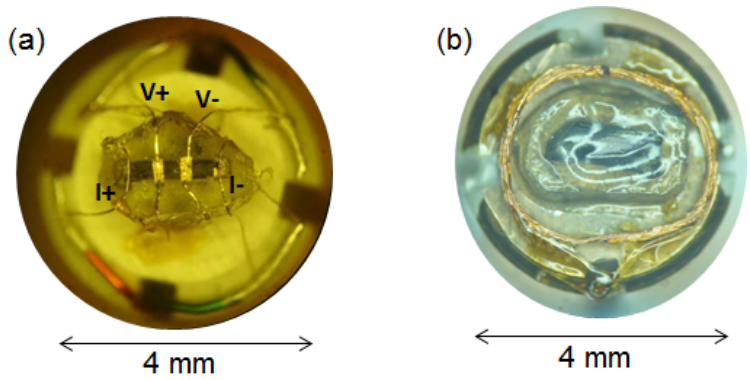

Figure 3.6: (a) Photo of the setting of four-wire resistivity measurement. The black part is a Ca_2RuO_4 sample and the surrounding transparent part is epoxy. The white part is the bottom piston of the pressure cell. Four Au wires put on the sample for resistivity measurement are connected to thicker and stronger Cu wires of diameter of 100 μm at the taper area of the piston, and the Cu wires are taken out through the hollows of the piston and the holes of the bottom lock bolt. (b) Photo of the setting of AC susceptibility measurement by the mini-coil method. The sample and the coil are put on a Be-Cu piston. The coil wires of 20 μm diameter are taken out through one of the hollows of the piston and the holes of the bottom lock bolt. 3 Cu wires of 200 μm diameter are attached to the piston on the rest hollows with Ag paste and taken out through the rest holes of the bottom lock bolt.

pressure, DC method was adopted and current direction was reverted in order to cancel the thermoelectric voltage. We used a Source Meter 2401 (Keithley) for low-temperature measurement, whereas a DC current source 7651 (Yokogawa) and a Multimeter 2000 (Keithley) was used for room-temperature measurement. We constructed a probe by ourselves (Fig. 3.7) for resistivity measurements using a SQUID magnetometer system (MPMS, Quantum Design) for temperature control and field application. A Cernox thermometer was attached above the pressure cell and temperature was monitored using a Temperature Monitor 218 (Lakeshore). For the magnetoresistance measurement, magnetic field was applied parallel to the pressure direction. The accuracy of the field alignment was better than 5 degrees.

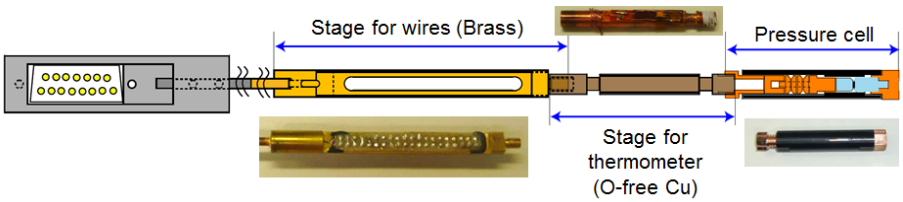

Figure 3.7: Schematic figure and photo of the probe for four-wire resistivity measurement using a SQUID magnetometer system (MPMS, Quantum Design).

3.2.2 AC susceptibility

We performed two kinds of AC susceptibility χ_{AC} measurement: the big-coil and mini-coil methods. I established the mini-coil method in order to get greater signal by improving the filling factor.

As the common feature of these methods, the temperature dependence of the AC susceptibility $\chi_{AC}(T) = \chi'(T) - i\chi''(T)$ was measured with a mutual inductance method using a Lock-in-amplifier SR830 (Stanford Research Systems) and ^{3}He cryostat Heliox VL (Oxford Instruments). χ_{AC} is related to the read-out voltage of the LIA ($V_{LIA} = V_x + iV_y$) as $\chi_{AC} = -iC_1V_{LIA}/fH^0_{AC} + C_2$. Here, H^0_{AC} and f are the amplitude and frequency of the applied AC magnetic field, and C_1 and C_2 are complex coefficients. Since we performed AC susceptibility measurement in order to clarify the UAP effect on SC properties of Sr_2RuO_4 whose T_c is about 1.5 K under ambient condition, the values of C_1 and C_2 were chosen so that $\chi'(4\text{ K}) = 0$ and $\chi'(0.3\text{ K}) = -1$ under ambient pressure and zero DC magnetic field for each sample; thus $|\chi'|$ corresponds to the AC shielding fraction. For the χ_{AC} curves under finite pressure or finite DC field, C_1 and C_2 determined under 0 GPa and 0 T were used. χ'' corresponds to energy dissipation. Both the AC magnetic field H_{AC} and the DC magnetic field H_{DC} were applied parallel to the pressure direction The accuracy of the field alignment was better than 5 degrees.

Big-coil method

Figure 3.8 represents the setting of the big-coil method. In the big-coil method, the longer pressure cell was used and both the pick-up and excitation coils were set outside the cell. The pick-up coil has cancellation part in which wires are wound in the inverse way. RuO_2 thermometers were put at the top of ^{3}He pot, the top of the coil, and the bottom of the pressure cell, and we confirmed that the difference among these temperatures is less than 5 degrees.

Mini-coil method

As described in Chap. 3.1.4, the area perpendicular to the pressure direction is smaller in samples for in-plane UAP than in samples for out-of-plane UAP, because Sr_2RuO_4 crystals cleave easily along the *ab* plane. As a result, the signal obtained with the big-coil method is smaller for samples for in-plane UAP because of their smaller filling factors. In order to solve the problem, I established the technique to put a pick-up coil inside the UAP cell and improve the filling factor; This is what we call the mini-coil method. For example, when the sample area is 2.0×0.5 mm^2 and the diameter of the pick-up coil is 2.5 mm, the filling factor is 20%: the filling factor is improved by more than 15 times compared with the big-coil case (1.3%).

The setting of the mini-coil method is described in Fig. 3.6(b). The shorter pressure cell was used in this method: polybenzimidazole is chosen as the material of the outer body in order to avoid eddy current, whereas Be-Cu is selected as the material of the other parts for better thermal link. In this method, the height of the pick-up coil should be shorter than the sample thickness for the coil not to be pressed by the pistons. Therefore, in order to increase the turn number, thin Cu wire of 20 μm diameter is used. The pick-up coil does not have cancellation part because of the limited space. The coil wires as well as Cu wires of 200 μm diameter for the thermal link between the bottom piston and ^{3}He pot were taken out through the hollow of the bottom piston

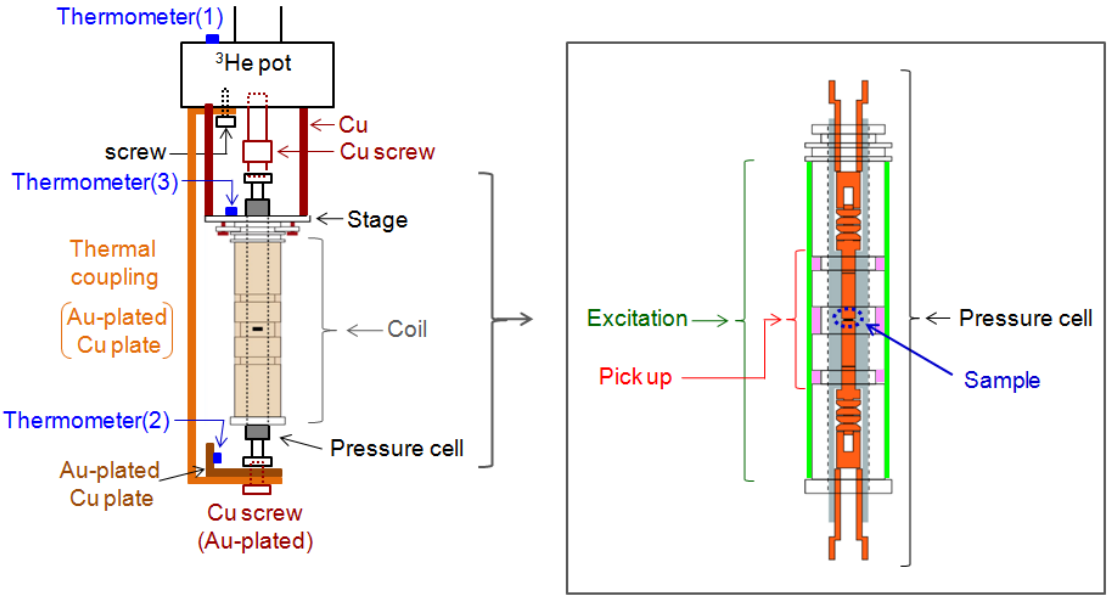

Figure 3.8: Schematic figure of the setting of AC susceptibility measurement in the big-coil method. The pick-up coil has three parts: without a sample, the voltage induced in the middle coil is cancelled out by the voltage induced in the top and bottom coils, because the top and bottom coils are wound in the inverse way compared with the middle coil.

and the hole of the bottom lock bolt. Moreover, sheets made of braided Cu wires surrounded the pressure cell and were connected to ^{3}He pot for thermal link.

3.2.3 Magnetization

Magnetization M was measured with a SQUID magnetometer (MPMS, Quantum Design). The magnetic field direction is parallel to the pressure direction. The accuracy of the field alignment was better than 5 degrees. To extract the SQUID response originating from the sample, the separately measured background signal was subtracted from the raw signal. For the background measurement, epoxy (Stycast 1266) with dimensions similar to those of the sample was used.

Chapter 4

Uniaxial pressure effects on Ca_2RuO_4

4.1 *In-plane* anisotropy of the uniaxial-pressure effect

4.1.1 Short summary

We investigated in-plane anisotropy of the UAP effect on Ca_2RuO_4 by measuring the resistance and magnetization, with a expectation that metal-insulator transition is induced: with UAP applied along the *ab* plane, samples are expected to expand along the *c* axis and to exhibit metallic behavior. We applied pressure either parallel to the in-plane Ru-O bond of RuO_6 octahedra (we denote this as the $[100]_T$ direction using the tetragonal notation) or diagonal to the Ru-O bond (the $[110]_T$ direction). From both resistivity and magnetization measurements, we clarified that a FM-M state with T_{FM} of 12 K is induced by $P_{\parallel[100]T}$ of 0.4 GPa or $P_{\parallel[110]T}$ of 0.2 GPa. Thus, we succeeded in inducing the FM-M phase at lower critical pressure than by hydrostatic pressure (0.5 GPa). This result indicates that the flattening distortion of the RuO_6 octahedra is more easily released by in-plane UAP. In addition to the anisotropy of the critical pressure of the FM-M phase, FM component of the magnetization exhibits anisotropy: although the magnetization increases monotonically with pressure diagonal to the orthorhombic principal axes, the magnetization exhibits peculiar dependence on pressure along the in-plane orthorhombic principal axes. This peculiar dependence can be explained by a qualitative difference between the UAP effects along the orthorhombic *a* and *b* axes, as well as by the presence of twin domain structures. We have also revealed that the B-AFM phase appears under $P_{\parallel[100]T}$ above 0.6 GPa or $P_{\parallel[110]T}$ above 1.3 GPa coexisting with the A-AFM phase. These striking anisotropic behavior demonstrates that the UAP is a powerful tool to control electronic states of layered oxides.

4.1.2 Resistivity under UAP

Figure 4.1 displays the temperature dependence of the four-wire resistance of Ca_2RuO_4 under $P_{\parallel[100]T}$. Below 0.2 GPa, $R(T)$ exhibits typical insulating behavior fitted well with the activation-type formula $R(T) \propto \exp(\Delta/2T)$ with Δ = 4000-5000 K, which is similar to that under ambient pressure [1, 72, 8, 73]. At 0.3 GPa, the resistance divergence is strongly reduced, suggesting the emergence of the metallic phase in a certain portion of the sample. Above 0.4 GPa, a peak in $R(T)$ (inset of Fig. 4.1) and large negative magnetoresistance (Fig. 4.2) are observed at around 12 K,

which are typical behavior of itinerant ferromagnets. Step-like changes of $R(T)$ are attributable to microcracks in the sample. We comment here that an accurate estimation of resistivity in high pressure is rather difficult due to the coexistence of the metallic and insulating phases, reflecting the first-order nature of the Mott transition, as well as due to microcracks in the sample. For a brief comparison, the resistance value of 1 kΩ at 0.1 GPa and 300 K (see Fig. 4.1) corresponds to ∼ 5 Ωcm according to a simple estimation based on the sample dimensions. This value is consistent with the reported value of the resistivity ρ_{ab} = 4 Ωcm at ambient pressure and 300 K. [8]

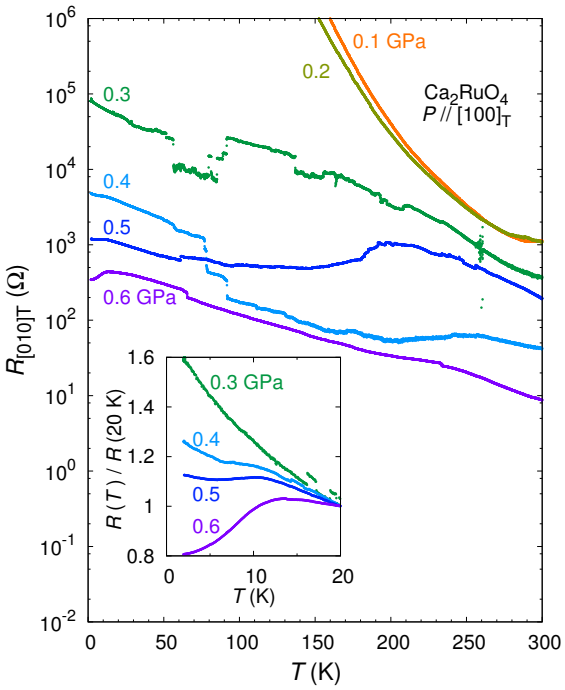

Figure 4.1: Temperature dependence of the four-wire resistance $R_{[010]T}$ of Ca_2RuO_4 under $P_{\|[100]T}$ measured in a cooling process. The inset represents the temperature dependence of $R_{[010]T}$ normalized by that at 20 K. The decrease of resistance below 12 K indicates an emergence of a FM order.

4.1.3 Magnetization under UAP

FM order is also observed in the magnetization M (the bottom inset of Fig. 4.2 and Fig. 4.3). The $M(H)$ curves exhibit clear hysteresis near $H = 0$ and saturation of M at higher fields. Although small hysteresis is observed even above T_{FM} because of the re-orientation of the canted AFM domains as previously reported [5], the size of the hysteresis loop steeply increases below about 10 K, indicating the emergence of the FM phase. In Fig. 4.3, the evolution of the FM order for $P_{\|[100]T}$ and $P_{\|[110]T}$ is compared in the $M(T)$ curves at 10 mT. Interestingly, we found that the FM state appears above 0.4 GPa for $P_{\|[100]T}$ whereas above 0.2 GPa for $P_{\|[110]T}$. These anisotropic critical pressures of the FM order are consistent with results of the resistivity measurements.

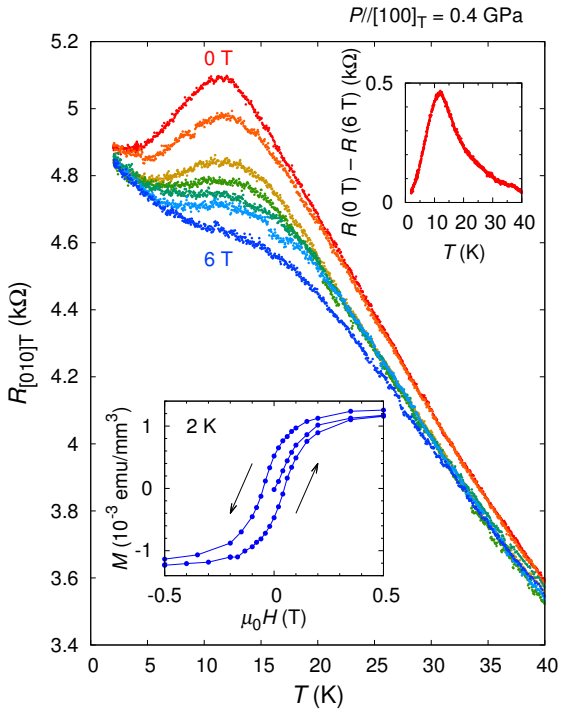

Figure 4.2: Temperature dependence of the four-wire resistance $R_{[010]\mathrm{T}}$ of Ca_2RuO_4 at $P_{\|[100]\mathrm{T}}$ of 0.4 GPa under magnetic field $H_{\|[100]\mathrm{T}}$. The sample is different from that of Fig. 4.1. All the resistivity data were taken with the field-cooling process. We have checked that $R(T)$ does not differ by cooling processes. The top inset displays the difference of the four-wire resistance between 0 and 6 T. The peak indicates $T_{\mathrm{FM}}\sim$ 12 K. The bottom inset displays the magnetic field $H_{\|[100]\mathrm{T}}$ dependence of the magnetization $M_{\|[100]\mathrm{T}}$ at 2 K under $P_{\|[100]\mathrm{T}}$ of 0.4 GPa. It exhibits a typical hysteresis corresponding to a FM ordering.

We also found that M(2 K)−M(30 K) in field-cooling (FC) process, which indicates magnetization component due to the FM order, exhibits anisotropic pressure dependence as shown in Fig. 4.3(e) and (f). This quantity increases almost monotonically with $P_{\|[100]\mathrm{T}}$. In contrast, under $P_{\|[110]\mathrm{T}}$ it first increases from 0.2 to 0.4 GPa, then decreases from 0.4 to 1.2 GPa, and increases again above 1.2 GPa.

We also detected AFM transitions in the $M(T)$ curves at 5 T (Fig. 4.4). At ambient pressure, $M(T)$ exhibits a peak at 115 K as a result of the A-AFM transition [2]. With increasing $P_{\|[100]\mathrm{T}}$ or $P_{\|[110]\mathrm{T}}$, the peak structure attributable to the A-AFM transition is retained. In addition, under $P_{\|[100]\mathrm{T}}$ above 0.6 GPa or $P_{\|[110]\mathrm{T}}$ above 1.3 GPa, a shoulder-like structure appears at around 140 K. Previous P_{hydro} studies revealed that a transition to another AFM state, the B-AFM state, occurs at T_{AFM} = 145 K between 0.2 and 0.8 GPa [6, 7]. With an analogy to the P_{hydro} result, the shoulder-like feature observed in our study is also interpreted as the emergence of the B-AFM insulating state. We emphasize that the onset critical pressure of the B-AFM state is highly anisotropic.

We note that the coexistence of the FM-M and AFM insulating phases is attributable to the

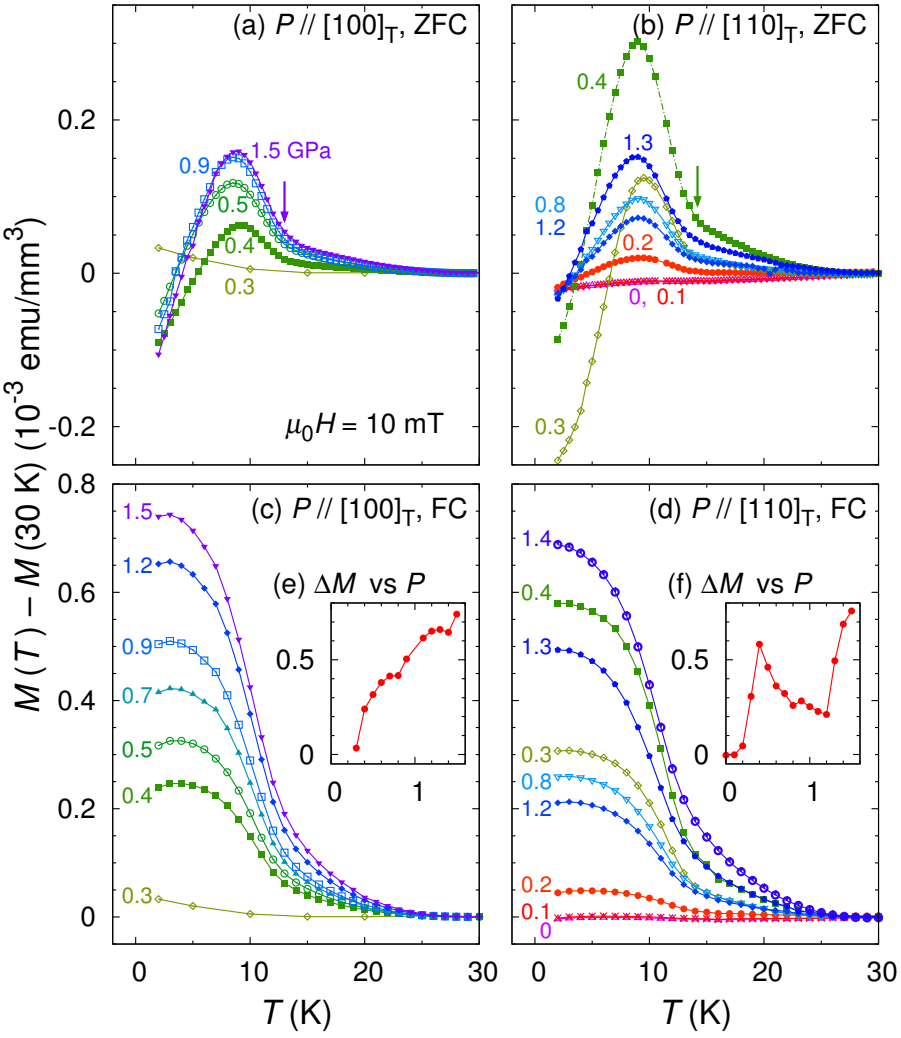

Figure 4.3: Development of the magnetization M measured with a field of 10 mT parallel to the pressure for (a)(c) $P_{\parallel[100]\mathrm{T}}$ and (b)(d) $P_{\parallel[110]\mathrm{T}}$. The panels (a) and (b) presents data taken with the warming process after zero field cooling (ZFC), and the panels (c) and (d) presents data with the field cooling (FC). The insets represent the pressure dependence of $\Delta M = M(2\ \mathrm{K}) - M(30\ \mathrm{K})$ in FC for (e) $P_{\parallel[100]\mathrm{T}}$ and (f) $P_{\parallel[110]\mathrm{T}}$. The units of the vertical and horizontal axes are 10^{-3} emu/mm^3 and GPa, respectively.

first-order nature of the transition as well as experimentally inevitable inhomogeneity of the lattice distortion under pressure. Similar coexistence is reported in thin film and P_{hydro} studies [6, 7, 15].

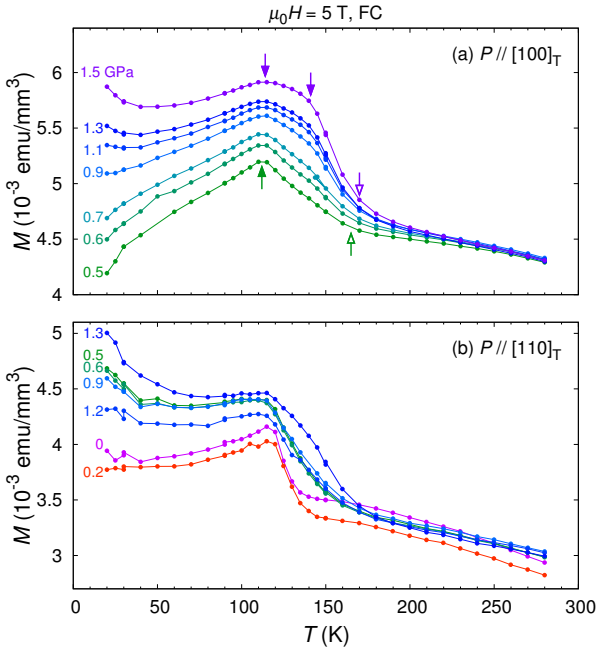

Figure 4.4: Temperature dependence of the magnetization M measured with a field of 5 T parallel to the pressure in field-cooling process for (a) $P_{\parallel[100]_T}$ and (b) $P_{\parallel[110]_T}$. The closed arrows around 115 K and 140 K indicate the peak and shoulder structures, corresponding to the A-centered and B-centered AFM transitions, respectively. The open arrows present the onset of the AFM orders.

4.1.4 Phase diagram

For analyzing the evolution of magnetic states by in-plane UAPs, we adopt two definitions for T_{FM} based on the magnetoresistance or magnetization. (1) For one definition, T_{FM} is determined as the temperature where $\Delta R \equiv R(0\ \mathrm{T}) - R(6\ \mathrm{T})$ exhibits a maximum as shown in the top inset of Fig. 4.2, because ΔR is related to the strength of the ferromagnetic fluctuation, which should be maximized at T_{FM}. (2) For the other, T_{FM} is determined as the temperature where $M(T)$ at 10 mT in ZFC process exhibits an abrupt increase, as shown by the arrows in Fig. 4.3(a,b). T_{FM} of two definitions takes almost the same values for the both pressure directions as shown in Fig. 4.5. The value of T_{FM}, ∼12 K, is very similar to that under P_{hydro} between 0.5 and 2.5 GPa [74, 8, 7]. We emphasize that the critical pressure of the FM-M phase under in-plane UAP is substantially smaller than that under P_{hydro}: In particular, the critical pressure under $P_{\parallel[110]_T}$ (0.2 GPa) is less than half of that under P_{hydro} (0.5 GPa). This fact demonstrates that the in-plane UAP is indeed effective for changing the electronic state of Ca_2RuO_4.

For the in-plane UAP effects on the AFM phases, we define three characteristic temperatures found in the magnetization at 5 T: the onset temperature of magnetization increase, the temperature of magnetization peak, and the temperature of the shoulder-like structure (Fig. 4.4). They are considered to indicate the onset temperature of an AFM transition T_{AFM}^{onset}, the ordering temperatures of the A- and B-AFM phases T_{A-AFM} and T_{B-AFM}, respectively. We found that T_{A-AFM}

and T_{B-AFM} do not vary with $P_{\|[100]T}$ or $P_{\|[110]T}$ in the present pressure range once they start to be observed. In contrast, T_{AFM}^{onset} exhibits substantial pressure dependence. We infer that T_{AFM}^{onset} is a characteristic temperature of the development of short-range magnetic correlation above the underlying second-order AFM transition temperatures. We attribute the increase of T_{AFM}^{onset} with increasing $P_{\|[100]T}$ or $P_{\|[110]T}$ to the appearance of a small fraction of the B-AFM order. The enhancement starts at 0 GPa under $P_{\|[100]T}$ whereas at 0.2 GPa under $P_{\|[110]T}$.

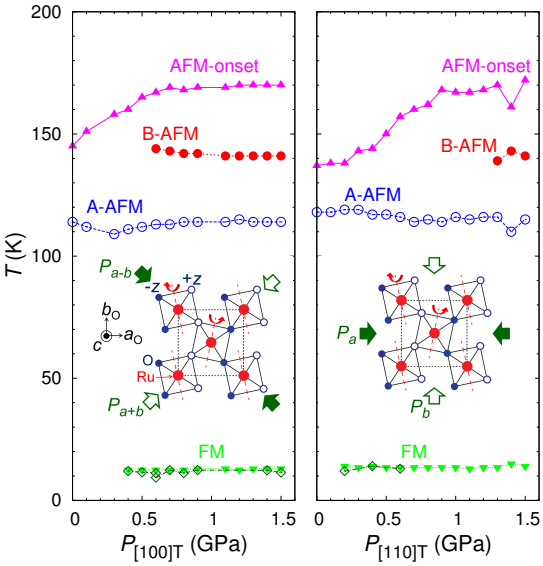

Figure 4.5: Pressure dependence of T_{FM} and T_{AFM} for (a) $P_{\|[100]T}$ and (b) $P_{\|[110]T}$. Diamonds and reversed triangles denote T_{FM} determined from magnetoresistance and magnetization, respectively. Triangles, open circles, and closed circles indicate T_{AFM}^{onset}, T_{A-AFM}, and T_{B-AFM}, respectively. The insets schematically describes the RuO_2 plane with the UAP. The broken lines denote the tilting axes. Because of the tilting, half of the O ions described with the open circles are located above the undistorted RuO_2 plane, while the others with the closed circles below the plane. Dotted lines indicate a unit cell.

To check the reproducibility, we have measured three samples for $P_{\|[100]T}$ (one for M and two for R) and other three samples for $P_{\|[110]T}$ (one for M and two for R). For $P_{\|[100]T}$, all samples provide consistent results. For $P_{\|[110]T}$, we obtain consistent results except for one sample for R measurement, attributable to difference in the crystal mosaic structures that we will describe in Chap. 4.1.5.

4.1.5 Discussion

In this subsection, we discuss the origin of the anisotropic pressure response of the electronic state of Ca_2RuO_4. In particular, while the response of the magnetization to $P_{\|[100]T}$ is rather monotonic and qualitatively similar to that to P_{hydro}, that to $P_{\|[110]T}$ is unusual in two points: (1) The FM magnetization increases twice, first between 0.1 and 0.4 GPa and then above 1.2 GPa (Fig. 4.3(d)). (2) The clear signature of the B-AFM phase is observed at substantially higher

pressure than the FM-M phase (Fig. 4.4(b)). This is rather surprising because under P_{hydro} the B-AFM phase emerges at lower pressures than the FM-M phase and these two phases coexist over a wide pressure range [6, 7].

It is known that release of the flattening distortion is a necessary condition for the FM-M phase. Importantly, the flattening is closely related to the orthorhombicity: there is a strong orthorhombicity with $a/b \sim 0.98$ in the presence of the flattening whereas a/b is about 1.00 in its absence [5, 6]. Here a and b are the orthorhombic in-plane lattice constants. Therefore, it is naturally expected that the FM-M phase is favored by $P_{\|b}$ through the reduction of orthorhombicity. In a microscopic viewpoint, because the b-axis pressure should not couple to tilting or rotation distortions, the pressure along the b axis is exected to shorten the in-plane Ru-O length directly and to force the RuO_6 octahedra to elongate along the c axis more effectively as described in Fig. 4.6. For the other in-plane pressure directions, the strain is absorbed by the enhancement of the tilting or/and rotation and only slightly affects the Ru-O bond lengths.

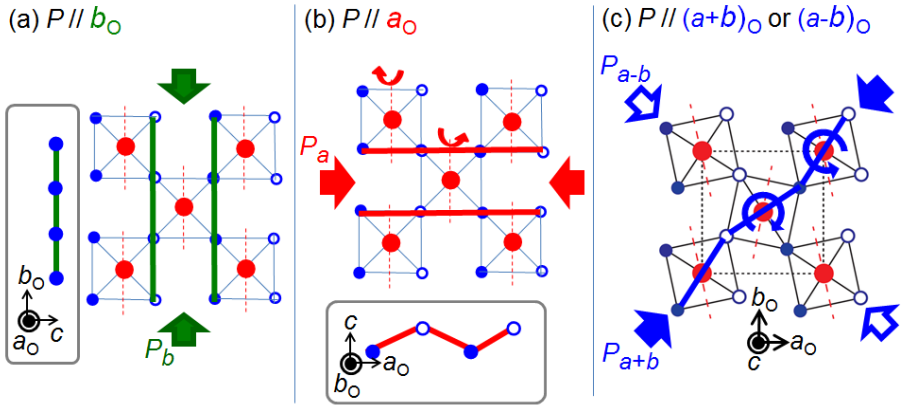

Figure 4.6: Lattice distortions expected to be induced under (a) $P_{\|b}$, (b) $P_{\|a}$, and (c) $P_{\|(a+b)}$ or $P_{\|(a-b)}$. Orthorhombic notation is used here. The main figures schematically describes the RuO_2 plane. For simplicity, here we ignore the rotation of RuO_6 octahedra around the c axis at the initial zero-pressure state and consider the lattice distortions induced by an in-plane UAP. The broken lines denote the tilting axes. Because of the tilting, half of the O ions described with the open circles are located above the undistorted RuO_2 plane, while the others with the closed circles below the plane. Dotted lines in the panel (c) indicate a unit cell. (a) Under $P_{\|b}$, the Ru-O bond length along the b axis is expected to be shortened, and as a result RuO_6 octahedra would elongate along the c axis in order to keep octahedra volume constant. (b) Under $P_{\|a}$, the tilting distortion would be enhanced first like a folding screen, because it seems easier than to shorten the Ru-O bond length along the a axis. (c) Under $P_{\|(a+b)}$ or $P_{\|(a-b)}$, the rotation distortion is expected to be induced first.

For understanding the observed pressure responses, we need to consider the presence of orthorhombic crystalline twin domains exemplified in Fig. 4.7. $P_{\|[100]\mathrm{T}}$ corresponds to either $P_{\|(a+b)}$ or $P_{\|(a-b)}$ depending on domains (the left inset of Fig. 4.5). However, since the effect on the lattice is expected to be equivalent between $P_{\|(a+b)}$ and $P_{\|(a-b)}$, the UAP effect for $P_{\|[100]\mathrm{T}}$ should be the same for both domains. The observed monotonic pressure dependence of the magnetization for

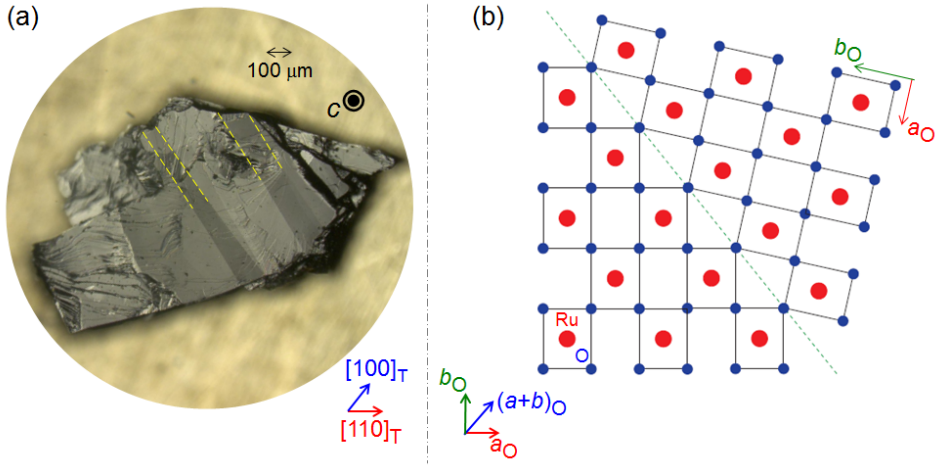

Figure 4.7: (a) Photo of the orthorhombic twin domains of Ca_2RuO_4 taken with a polarized optical microscope. Yellow broken lines denote domain boundaries: the darkness of the left side of the line is different from that of the right side because of the difference of reflectivity due to the twin domains. Note that the color of the image is not modified except for the addition of the yellow lines. (b) Schematic figure of the orthorhombic twin domains of Ca_2RuO_4. Red and blue circles represent Ru and O ions, respectively. Arrows denote the orthorhombic a or b axes. Broken line represents the domain boundary: the twin boudaries run along the orthorhombic $(a + b)$ axis.

$P_{\|[100]T}$ is attributable to such absence of the domain effect. In contrast, the presence of a domain structure is expected to play a key role under $P_{\|[110]T}$: Smaller critical pressure of the FM-M phase is expected for the domain under $P_{\|b}$ (the b-domain) than for the domain under $P_{\|a}$ (the a-domain) as we have described. Therefore, the non-monotonic pressure dependence of the magnetization can be understood naturally: First, the FM-M phase is induced at $P_{\|[110]T} = 0.2$ GPa within the b-domain possibly with the absence of the B-AFM phase, giving rise to the initial overall increase of the magnetization. The decrease of magnetization above 0.4 GPa (Fig. 4.3(f)) is likely to occur also in the b domain. With increasing pressure, the FM-M phase is induced within the a-domain above 1.2 GPa accompanied by the B-AFM phase, resulting in the second increase of the magnetization below 12 K (Fig. 4.3(f)) and the appearance of a shoulder-like structure at around 145 K (Fig. 4.4(b)). This extraordinary domain selectivity highlights the uniqueness of UAP that cannot be systematically explored with P_{hydro}.

We note that the essential electronic difference between the A- and B-AFM phases is in the orbital occupation of four Ru 4d electrons [75, 24]. In both phases each of three electrons occupies the xy, yz, and zx orbitals respectively, due to Hund's coupling. The A-AFM phase is realized in the ferro-orbital state with the fourth electron occupying the xy orbital for all Ru sites, whereas the B-AFM phase is realized in an antiferro-orbital state with a partial xy-band occupation. The observed anisotropy of the critical pressure of the B-AFM phase should be related to this difference. Band calculation of Ca_2RuO_4 incorporating lattice distortions under in-plane UAPs is needed for further discussion.

4.2 Suppression of the insulating gap under *out-of-plane* uniaxial pressure

4.2.1 Short summary

We performed resistance measurement of Ca_2RuO_4 under out-of-plane UAP with a expectation that the insulating gap will increase because of the enhanced energy difference between *xy* and *yz*, *zx* orbitals of Ru 4*d* electrons. Surprisingly, the experimental result is opposite from the prediction: although the temperature dependence of the out-of-plane resistance remains insulating under $P_{\|c}$ up to 2.5 GPa, the insulating gap Δ is suppressed from 3000 K to 700 K. This result strongly suggests the possibility of a new metallic state in Ca_2RuO_4: the metallic state under out-of-plane UAP is probably induced by the enhanced band width caused by the suppression of the rotation or tilting distortion, whereas the metallic state under hydrostatic or in-plane uniaxial pressure is realized by the suppression of the crystal field splitting when the flatteing distortion is released.

4.2.2 Resistivity under UAP

Figure 4.8 represents the out-pf-plane UAP dependence of the two-wire resistance $R_{\|c}$ of Ca_2RuO_4 at room temperature. We note that the initial drop of resistance from 0 GPa to 0.2 GPa is mainly attributed to the improvement of the contact resistances between the sample and the piston and between the inner parts of the pressure cell, and thus this is not intrinsic. What is surprising is that the resistance continues to decrease up to 2.5 GPa. This result suggests the possibility that a metallic phase is induced or the insulating gap is suppressed in Ca_2RuO_4 under $P_{\|c}$ in contrast to the simple prediction described in Chap. 4.2.1.

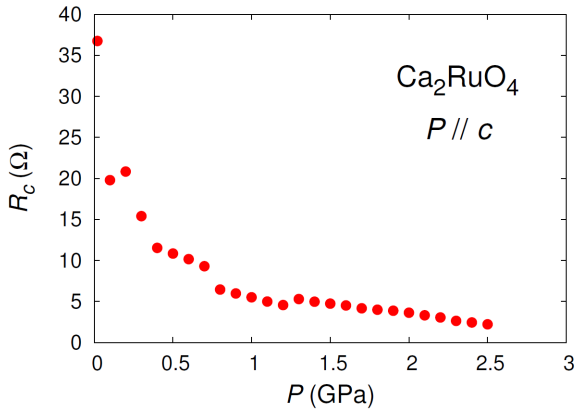

Figure 4.8: Out-of-plane UAP dependence of resistance $R_{\|c}$ of Ca_2RuO_4 at room temperature. Gradual decrease of the resistance up to 2.5 GPa seems to indicate the suppresion of the insulating gap, although the initial drop from 0 GPa to 0.2 GPa would be caused by an extrinsic contribution, which is the improvement of the contact resistances between the sample and the piston and between the inner parts of the pressure cell.

In order to check the reproducibility of this suppression of the resistance by $P_{\|c}$, we measured two-wire $R_{\|c}$ under $P_{\|c}$ for 11 Ca_2RuO_4 samples. The resistance decreased with $P_{\|c}$ for 5 samples, although it increased for 2 samples. For the other 4 samples, the resistance was unstable and did not exhibit clear pressure dependence. In order to reveal the out-of-plane UAP effect on the intrinsic resistance, we should consider the pressure dependence of extrinsic resistances; with increasing pressure, the measured value of resistance will be enhanced by cracks, whereas it will be suppressed by the improved electric contact between the sample and the piston and between the inner parts of the pressure cell. Since these two extrinsic contributions have opposite pressure dependence, it is difficult to clarify the out-of-plane UAP effect on Ca_2RuO_4 only from the pressure dependence of the two-wire out-of-plane resistance.

Therefore, we measured the temperature dependence of the resistance $R_{\|c}$ of Ca_2RuO_4 under $P_{\|c}$ of 2.5 GPa (Fig. 4.9). Metallic temperature dependence of R_c was not observed in the present pressure range up to 2.5 GPa. However, we have revealed the suppression of the insulating gap: the $R(T)$ data between 300 K and 100 K are fitted well with the activation-type insulating behavior,

$$R_c = R_0 \exp\left(\Delta/2k_BT\right) \tag{4.1}$$

giving $\Delta \approx 700$ K, which is substantially smaller than the gap obtained from the out-of-plane resistivity of a single crystal Ca_2RuO_4 at ambient pressure ($\Delta \approx 3000$ K [8]). The resistance below 100 K cannot be fitted with the activation-type behavior, eq. (4.1), and exhibits a much weaker divergence. This weakness of the increase of resistance on cooling also supports our conclusion that the electronic state of Ca_2RuO_4 tends to be closer to a metallic state by $P_{\|c}$.

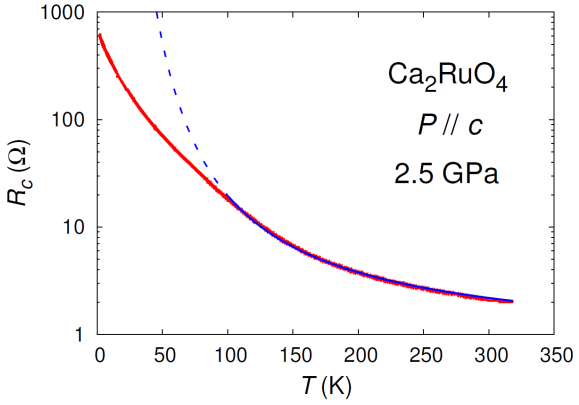

Figure 4.9: Temperature dependence of the out-of-plane resistance $R_{\|c}$ under $P_{\|c}$ of 2.5 GPa. Red line represents the experimental result measured with an AC current of 0.01 mA-rms at 7 Hz. Blue solid line indicates an activation-type curve within the fitting region, whereas dashed line outside the fitting region.

4.2.3 Discussion

Naively, it is expected that $P_{\|c}$ enhances the flattening distrotion of RuO_6 octahedra and increases the insulating gap Δ of Ca_2RuO_4. Surprisingly, however, the suppression of Δ was observed. We

consider that band width plays an important role for this unexpected behavior. As shown in the middle figure of Fig. 4.10, the insulating gap of Ca_2RuO_4 locates between the upper Hubbard band (UHB) originating from the *yz* and *zx* orbitals of Ru 4*d* electrons and the UHB originating from the *xy* orbitals. Therefore, the gap size Δ has the following relation:

$$\Delta = E_{\mathrm{crystal}} - W_{xy}/2 - W_{yz,zx}/2 \tag{4.2}$$

Here, E_{crystal} is the value of the crystal field splitting between the *xy*-UHB and the yz, zx-UHB. W_{xy} and $W_{yz,zx}$ are the band width of the *xy*-UHB and yz, zx-UHB, respectively. Since $P_{\|c}$ is expected to intensify the flattening distortion of RuO_6 octahedra along the *c* axis, E_{crystal} will be enhanced by $P_{\|c}$. Thus, for Δ to be suppressed, W_{xy} or $W_{yz,zx}$ or both should increase under $P_{\|c}$. If the rotation distortion of RuO_6 octahedra is weakened, the Ru-O-Ru bond angle on the *xy* plane approaches to 180 degrees, and the hybridization between the Ru *xy* orbital and the O *x* or *y* orbital increases resulting in wider W_{xy}. Similarly, both W_{xy} and $W_{yz,zx}$ will increase when the tilting distortion of RuO_6 octahedra is suppressed. Therefore, we consider that the rotation or tilting or both distortions are weakened in Ca_2RuO_4 under $P_{\|c}$ and the electronic state approaches to a metallic state, which is different from the metallic state which emerges as the result of the suppression of E_{crystal} by the elongation of RuO_6 octahedra along the *c* axis.

Let us comment on the possibility that a two-dimensional metallic state is already realized in the sample. Here, two-dimensional metallic state means a state where only the in-plane transport is metallic. Indeed, in the hydrostatic pressure experiments, it was reported that the *c*-axis resistivity ρ_c exhibits a non-metallic temperature dependence even in the metallic phase [8]. Therefore, in order to clarify whether a metallic phase is induced or only the insulating gap is suppressed, the in-plane resistivity of Ca_2RuO_4 under $P_{\|c}$ should be measured as a future issue. The four-wire method is appropriate for this measurement, because we would like to measure resistance under a condition in which extrinsic resistances do not decrease with pressure. Anyway, the electronic state of Ca_2RuO_4 under $P_{\|c}$ is really fascinating, because it probably approaches to a new metallic state which is different from the metallic state under hydrostatic or in-plane uniaxial pressure. Clarification of the ground state characteristics under $P_{\|c}$ is also important.

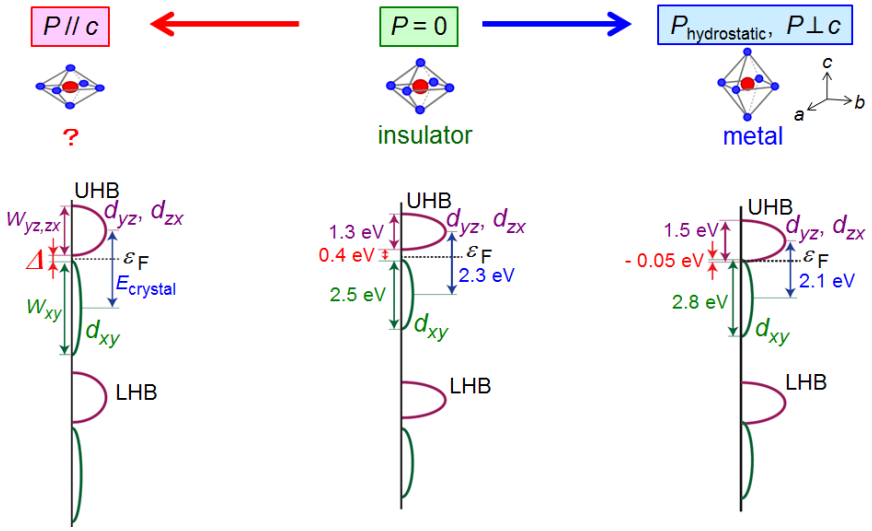

Figure 4.10: Schematic figure of the electronic states of Ca_2RuO_4 under ambient pressure (middle figure), out-of-plane UAP (left figure), and in-plane UAP or hydrostatic pressure (right figure). Here, Δ is the insulating gap and E_{crystal} is the value of the crystal field splitting between the xy-UHB and the yz, zx-UHB. W_{xy} and $W_{yz,zx}$ are the band width of the xy-UHB and yz, zx-UHB, respectively. Because of the flattening distortion of RuO_6 octahedra along the c axis, the energy level of the xy band is lower than that of the yz, zx band and the insulating state realizes in Ca_2RuO_4 under ambient condition. Under $P_{\|c}$, since Δ decreases despite the intensified flattening distortion, only W_{xy} or both W_{xy} and $W_{yz,zx}$ are considered to be enhanced by the suppression of the rotation or/and tilting distortion. Under hydrostatic or in-plane uniaxial pressure, which release the flattening distortion, the metallic state is induced by the suppression of E_{crystal}. For the middle and right figures, E_{crystal}, W_{xy} and $W_{yz,zx}$ are estimated from band calculation, optical conductivity, and X-ray spectroscopy [26, 76, 77, 78, 79, 80, 81]; based on the estimation, an insulating gap of 0.4 eV exists at Fermi level ϵ_F in the middle figure, whereas the xy-UHB and the yz, zx-UHB overlap by 0.05 eV in the right figure.

Chapter 5

Uniaxial pressure effects on Sr_2RuO_4

5.1 *In-plane* anisotropy of the uniaxial-pressure effect on Sr_2RuO_4

5.1.1 Short summary

We measured AC susceptibility of Sr_2RuO_4 with the mini-coil method under in-plane UAPs along the two distinct directions, $[100]_T$ or $[110]_T$, in order to obtain hints for conclusive evidence of the superconducting order parameter of Sr_2RuO_4 whose orbital part is expected to be two-component under ambient condition. Notably, by $P_{\|[100]T}$, the onset of supercondcuting transition temperature T_c is enhanced up to 3.3 K at only 0.05 GPa and remains 3.3 K up to 0.3 GPa. In contrast, the onset T_c is gradually enhanced by $P_{\|[110]T}$. These contrasting results suggest that $P_{\|[100]T}$ rather than $P_{\|[110]T}$ is favorable for inducing 3-K superconductivity (SC). Because it is observed that the shielding fraction around 3 K is suppressed after releasing the pressure, the 3-K SC under in-plane UAP should be mainly induced by elastic lattice distortion. Since crystal symmetry should be reduced by in-plane UAP, the orbital part of the superconducting order parameter of Sr_2RuO_4 is expected to be one-component in the 3-K SC realized by in-plane UAP, and to become two-component below a certain temperature. The double transition reflecting the existence of two different superconducting phases, the non-chiral SC at higher temperature and the chiral SC at lower temperature, was not observed in the imaginary part of the AC susceptibility.

5.1.2 AC susceptibility under UAP

Figure 5.1 represents the temperature dependence of the real part of the AC susceptibility of Sr_2RuO_4. We revealed that the in-plane UAP dependence of the onset T_c is highly anisotropic, as shown in the insets of Figs. 5.1 (a) and (b): the onset T_c is abruptly enhanced up to 3.3 K at only 0.05 GPa and remains 3.3 K for higher $P_{\|[100]T}$. In contrast, the onset T_c is gradually enhanced under $P_{\|[110]T}$. Moreover, compared with the $P_{\|[110]T}$ case, the superconducting transition is remarkably broadened under $P_{\|[100]T}$.

Previous studies on the Sr_2RuO_4-Ru eutectic, Sr_2RuO_4 under out-of-plane UAP, and Sr_2RuO_4 around dislocations suggest that Sr_2RuO_4 has the optimal T_c of 3.3 K and this 3-K SC may have

quality different from the 1.5-K SC under ambient condition [66, 64, 32, 82]. In this study, we have newly clarified that 3-K SC is induced in Sr_2RuO_4 also by in-plane UAP and $P_{\|[100]T}$ is more favorable than $P_{\|[110]T}$ for inducing the 3-K SC.

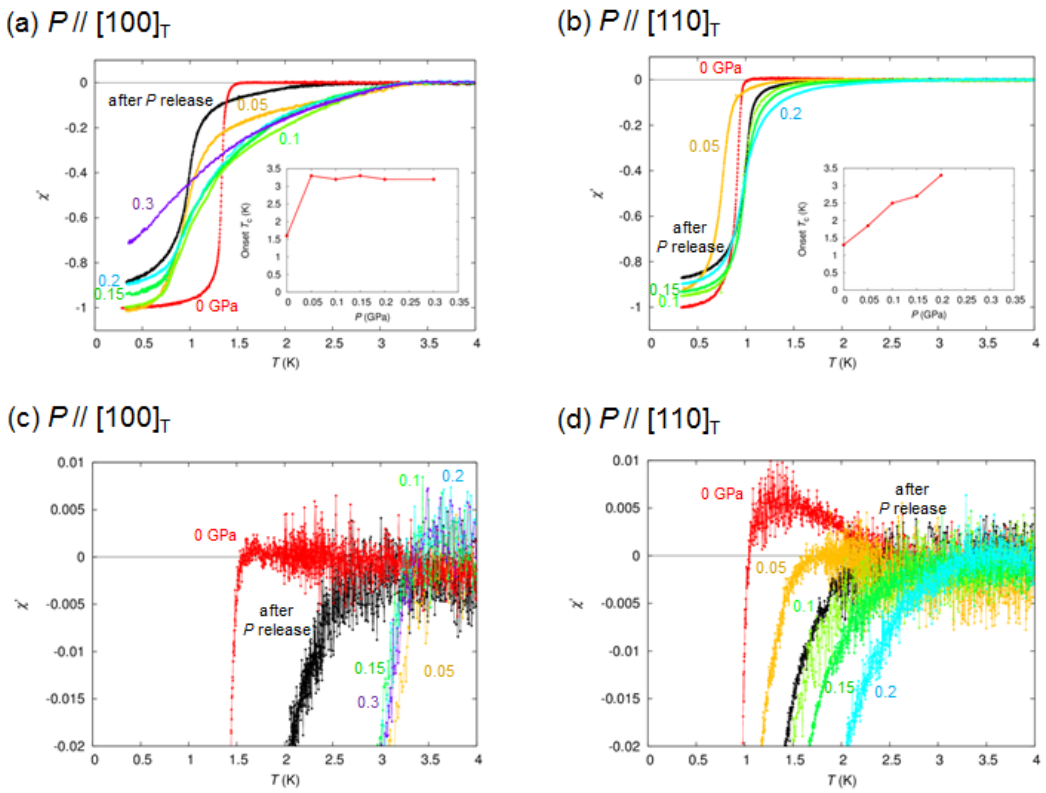

Figure 5.1: Temperature dependence of the real part of the AC susceptibility of Sr_2RuO_4 under (a)(c) $P_{\|[100]T}$ and (b)(d) $P_{\|[110]T}$ measured with an AC magnetic field of 20 mOe-rms. The panels (c) and (d) are enlarged views around the superconducting onset. Black curves show the data taken about one week after releasing pressure from 0.3 GPa for $P_{\|[100]T}$ and from 0.2 GPa for $P_{\|[110]T}$. The insets of Fig. (a) and (b) represent the pressure dependence of the onset T_c under $P_{\|[100]T}$ and $P_{\|[110]T}$, respectively, clarifying the contrasting behavior between them.

We also measured the AC susceptibility of Sr_2RuO_4 at about one week after releasing pressure from 0.3 GPa for $P_{\|[100]T}$ and from 0.2 GPa for $P_{\|[110]T}$, as shown in Figs. 5.1 and 5.2. In both $P_{\|[100]T}$ and $P_{\|[110]T}$ cases, the onset T_c is suppressed down to about 2.5 K and the shielding fraction is remarkably suppressed between the original bulk T_c at ambient pressure and 3.3 K. These results indicate that the 3-K SC under in-plane UAPs is induced mainly by an elastic distortion, although some additional contribution of plastic distortion like a dislocation [82] cannot be completely excluded because the onset T_c after releasing pressure is still higher than the original value.

Figure 5.2 represents the temperature dependence of the imaginary part of the AC susceptibility of Sr_2RuO_4. Peak structure originating from energy dissipation is not clearly observed at

around 3 K at least in this resolution. Double transition below 1.5 K at 0.05 and 0.1 GPa probably results from T_c distribution caused by the inhomogeneity of lattice distortion.

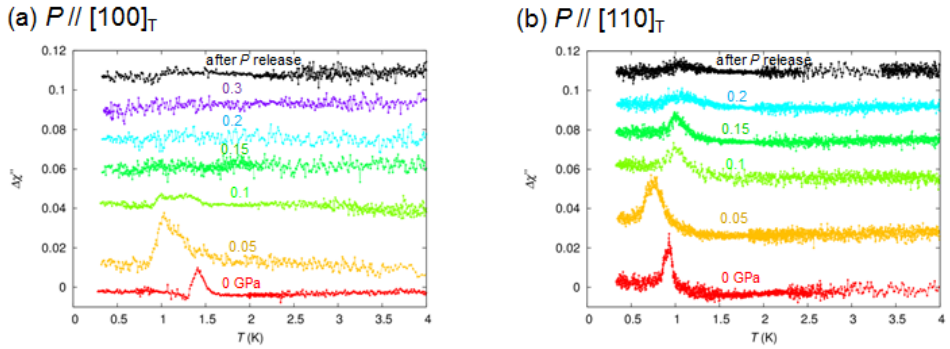

Figure 5.2: Temperature dependence of the imaginary part of AC susceptibility of Sr_2RuO_4 under (a) $P_{\|[100]T}$ and (b) $P_{\|[110]T}$ measured with a AC magnetic field of 20 mOe-rms.

As shown in Figure 5.3, the 3-K SC induced by $P_{\|[100]T}$ is robust against changes in the amplitude of AC magnetic field. This tendency was the same also in the case of $P_{\|[110]T}$.These results are similar to that of the 3-K SC induced by out-of-plane UAP, but different from that of the 3-K SC in Sr_2RuO_4-Ru eutectic crystal [68], suggesting that the 3-K SC induced in Sr_2RuO_4 by in-plane UAPs is not filamentary.

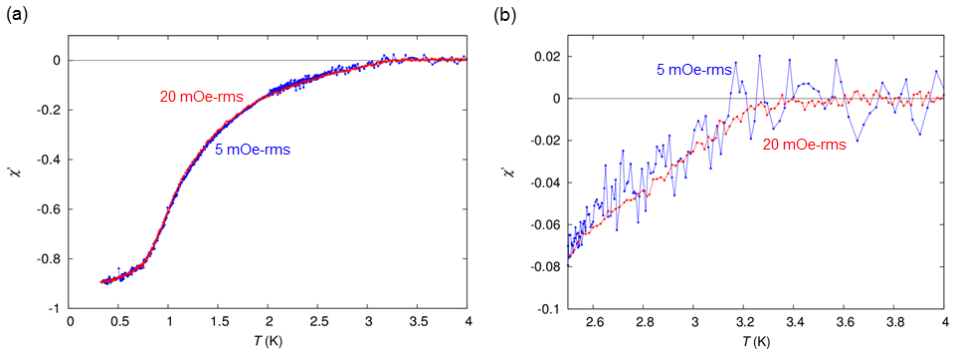

Figure 5.3: Difference between 5 and 20 mOe-rms of the temperature dependence of the real part of AC susceptibility of Sr_2RuO_4 under $P_{\|[100]T}$ of 0.2 GPa. The panel (b) is an enlarged view around the superconducting onset. Two curves are coincident well with each other, suggesting bulk-like SC.

5.1.3 Discussion

Similar to the present study, much larger enhancement of T_c is observed for the *strain* along $[100]_T$ than $[110]_T$, as shown in Fig. 5.4 [83]. The fact that unusual symmetric change in T_c for both compressive and expansive $[100]_T$ strains supports the two-component order parameter of

the SC in Sr_2RuO_4. The $[100]_T$ strain results of Ref. [83] may seem to be quantitavely different from our $P_{\|[100]T}$ results: as shown in Figs. 5.5 and 5.4, T_c is gradually enhanced and reaches only 1.9 K at −0.23 % *strain*, which corresponds to 0.23 GPa in our experiment according to the simplest estimation. We can naturally explain this different behavior by considering the difference of experimental setup: the pick-up coil of our measurements surrounds the entire sample as shown in Fig. 3.6 (b) and detects the whole magnetic signal originating from the sample, whereas the pick-up coil in the study of Ref. [83] is much smaller than a sample and detects only the magnetization of near the central region which is expected to be coherently distorted. Therefore, the superconducting transition observed in our study is dominated by strongly distorted region with higher T_c. In fact, as shown in Fig. 5.6, the resistivity measurements in the uniaxial *strain* experiments [84, 85] reveal that the sample under strain contain a part with much higher T_c than proved by the AC susceptibility. The qualitative difference between $[110]_T$ strain and pressure effects is a future issue: under $[110]_T$ compressive strain, T_c is suppressed, although the change is quite small.

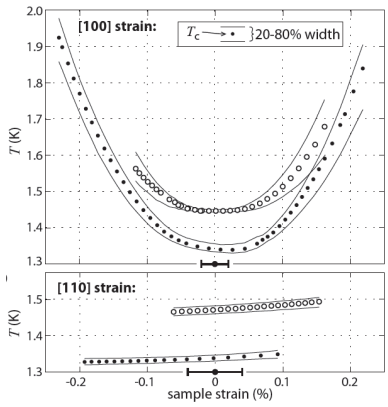

Figure 5.4: Uniaxial-*strain* dependence of superconducting transition temperature of Sr_2RuO_4 [83]. Negative and positive strains correspond to compressive and stretching strain, respectively.

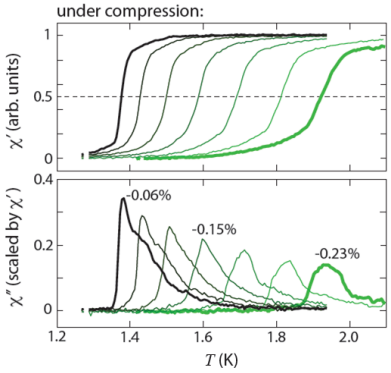

Figure 5.5: Temperature dependence of AC susceptibility of Sr_2RuO_4 under compressive uniaxial *strain* along the $[100]_T$ direction [83].

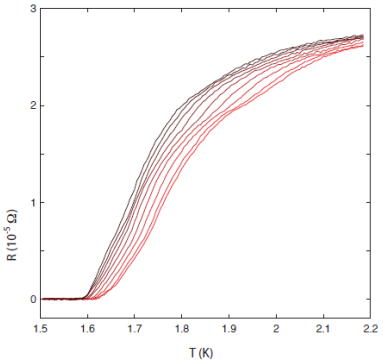

Figure 5.6: Temperature dependence of resistivity of Sr_2RuO_4 under compressive uniaxial *strain* along the $[100]_T$ direction [84]. The black left curve shows the data of zero strain and the red right curve shows the data of up to 0.06 % strain.

5.2 *Out-of-plane* uniaxial pressure effect on eutectic Sr_2RuO_4-Ru

5.2.1 Short summary

Superconducting transition temperature T_c of Sr_2RuO_4, which is 1.5 K under ambient condition, is known to be enhanced up to about 3 K by out-of-plane UAP [32] or by formation of Sr_2RuO_4-Ru eutectic crystal [29]. The former superconductivity (SC) can be called as $P_{\|c}$-originated 3-K SC, whereas the latter is called interfacial 3-K SC because previous studies indicate that the 3-K SC occurs around the interfaces between Sr_2RuO_4 and Ru. In order to clarify the difference between these 3-K SCs, we measured AC susceptibility and resistance of Sr_2RuO_4-Ru eutectic crystal under $P_{\|c}$. *H-T* phase diagrams determined from the temperature dependence of the AC susceptibility under various DC magnetic fields exhibit concave-up behavior with decreasing temperature both in $P_{\|c}$-originated SC and in interfacial SC, suggesting both SCs have granular-like properties. In contrast, resistance behavior highlights the difference bewteen $P_{\|c}$-originated SC and interfacial SC. Interestingly, sharp drop of resistance at about 1.5 K, which corresponds to the bulk T_c of Sr_2RuO_4 under ambient condition, is induced at 0.1 GPa and disappears again at 0.3 GPa. We consider that this non-monotonic behavior indicates that the spatial distribution of the 3-K SC changes from 0 GPa to 0.3 GPa.

5.2.2 AC susceptibility under UAP

Figure 5.7 represents the temperature dependence of the AC susceptibility χ_{AC} of Sr_2RuO_4-Ru under $P_{\|c}$= 0 and $P_{\|c}$= 0.5 GPa > P^*, where P^* is the characteristic pressure described below.

In a previous study [32], we revealed that the shielding fraction of 3-K SC in a Sr_2RuO_4-Ru eutectic crystal is enhanced by $P_{\|c}$ and properties of 3-K SC change at a critical pressure $P^* \sim$ 0.4 GPa in the following three points: the slope of the pressure dependence of the shielding fraction of 3-K SC becomes 12 times steeper above P^* (Fig. 5.8), shielding fraction increases below T_c of Ru (0.49 K) only above P^* (Fig. 5.9), and H_{AC}-sensitive behavior of 3-K SC disappears above P^* (Fig. 5.10).

Thus, we consider that the behavior at 0 GPa originates from the interfacial SC, whereas the behavior at 0.5 GPa reflects properties of the $P_{\|c}$-originated SC. An enlarged view around the superconducting onset is shown in Fig. 5.7(b). The shielding fraction between 1.7 K and 3.0 K is enhanced, consistent with previous reports [69, 68]. The decrease of the volume fraction at lower temperatures is attributable to partial destruction of SC due to excess or inhomogenuity of distortion as well as to cracks in the sample [32].

Next, we measured χ_{AC} of the same sample at 0.5 GPa under several DC magnetic fields (Fig. 5.11). In the $P_{\|c}$-enhanced shielding region ($0 < |\chi'| < 0.05$), $\chi'(T)$ curves exihibit parallel shift to lower temperature with increasing field (Fig. 5.11(b)). This behavior is different from the field response of χ_{AC} of the interfacial SC below $P^*_{\|c}$; the interfacial SC does not exhibit parallel shift, as exemplified in the region of $0 < |\chi'| < 0.6$ in Fig. 5.12 [31].

In order to illustrate the difference between the 3-K SC in Sr_2RuO_4-Ru above $P^*_{\|c}$ ($P_{\|c}$-originated SC) and that below $P^*_{\|c}$ (interfacial SC), we present in Fig. 5.13 the *H-T* phase diagram of these SCs. Figure 5.13 also contains the *H-T* phase diagram of the bulk SC of Sr_2RuO_4 at

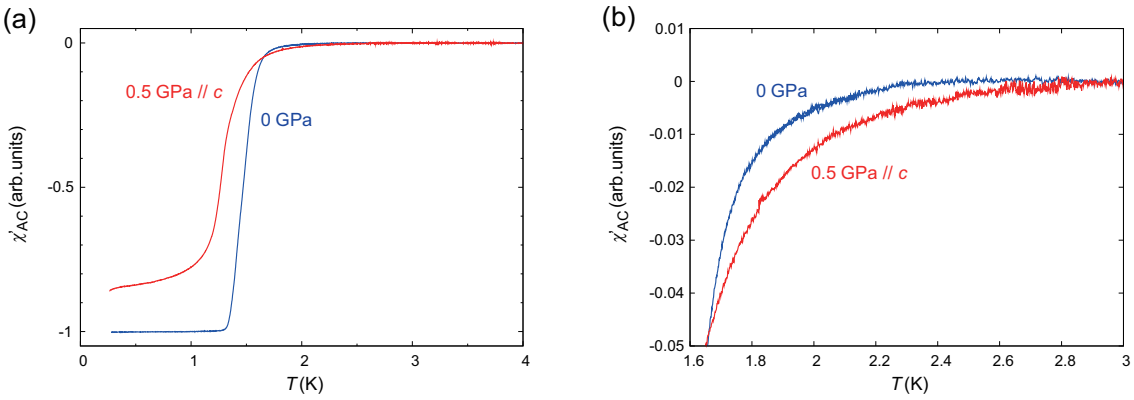

Figure 5.7: Zero-field temperature dependence of the real part of the AC susceptibility of Sr_2RuO_4-Ru under $P_{\|c}$= 0 and $P_{\|c}$= 0.5 GPa: (a) the overall behavior and (b) an enlarged view around the superconducting onset. These data were obtained with $\mu_0 H_{AC}$= 2 μT-rms and f = 293 Hz.

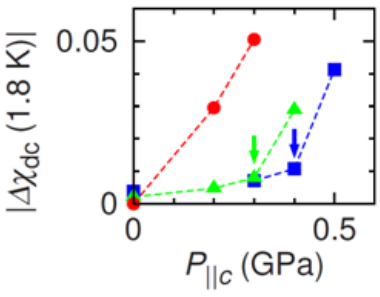

Figure 5.8: Out-of-plane UAP dependence of the DC shielding fraction of Sr_2RuO_4 and Sr_2RuO_4-Ru at 1.8 K and 2 mT [32]. Red and blue points represent the results of Sr_2RuO_4 and Sr_2RuO_4-Ru, respectively. Green points represent the results of a Sr_2RuO_4 crystal whose number of Ru inclusions is between that of Sr_2RuO_4 and Sr_2RuO_4-Ru eutectic. The arrows indicate critical pressure P^*.

$P_{\|c}$ = 0 [86]. All the H-T phase diagrams are determined by χ_{AC}. We define superconducting transition temperature T_c in the following two ways: T_c^{cross} is defined as the temperature of the intersection of the extrapolations of the most rapidly changing part of χ' and the normal state χ' as shown in Fig. 5.11(b), and T_c^{onset} is defined as the temperature at which χ' reaches −0.005. We used the steepest slope in $0 < |\chi'| < 0.05$ to determine T_c^{cross} of $P_{\|c}$-originated SC, so that T_c^{cross} captures the characteristics of the $P_{\|c}$-originated SC. For the same reason, the steepest slope in $0 < |\chi'| < 0.6$ is used for T_c^{cross} of the interfacial SC.

We have revealed that the H-T curves of the $P_{\|c}$-originated SC and the interfacial SC are concave up with decreasing temperature, while the H-T curves of the bulk SC of Sr_2RuO_4 is convex up. We also clarified that the slopes of the H-T curve of the $P_{\|c}$-originated SC are smaller than those of the interfacial SC resulting in a crossing at around 0.04 T. Note that these features

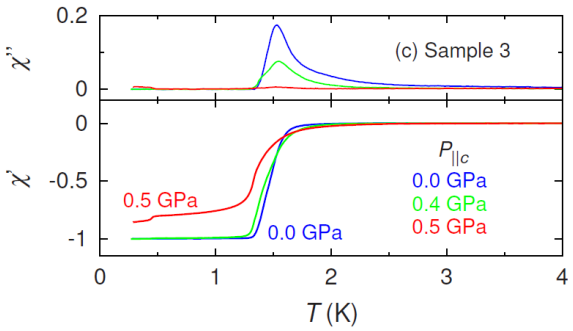

Figure 5.9: Temperature dependence of the AC susceptibility of Sr_2RuO_4-Ru under different $P_{\|c}$'s measured with $\mu_0 H_{AC}$= 2 μT-rms and 293 Hz [32]. Under 0.5 GPa, a jump is observed at 0.49 K both in the imaginary part χ'' and the real part χ'.

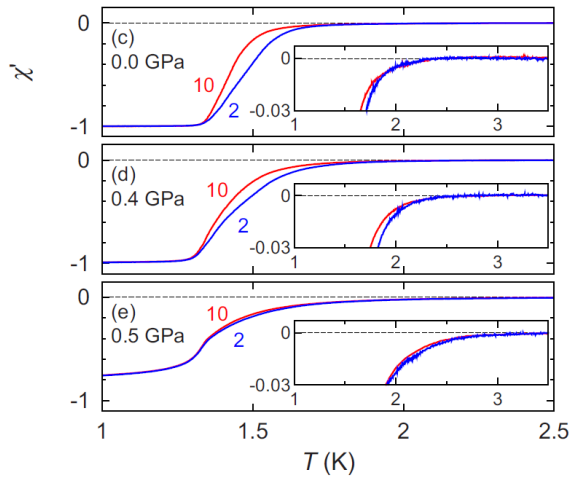

Figure 5.10: Temperature dependence of the real part of the AC susceptibility of Sr_2RuO_4-Ru under $P_{\|c}$for $\mu_0 H_{AC}$ of 2 and 10 μT-rms (293 Hz) [32]. The insets are enlarged views near the onset. The dashed lines mark $\chi' = 0$.

are not affected by the definitions of T_c.

It is known that H-T curves of granular superconductors exhibit concave-up behavior with decreasing temperature. A calculation of the effective critical field H_j of an assembly of intergranular Josephson junctions revealed that H_j exhibits $1/T$ dependence in the vicinity of $T_c(H{=}0)$ [87, 88]. In order to examine this possibility, we fitted the equation

$$\mu_0 H_j(T) = a\left(\frac{1}{T} - \frac{1}{T_c(H=0)}\right) \tag{5.1}$$

to the data in the range $0.5T_c(H{=}0) < T < T_c(H{=}0)$. The well-fitted results shown in Fig. 5.13 imply that both the $P_{\|c}$-originated SC and the interfacial SC have granular-like features. The difference in the slope of the H-T curve is possibly related to certain changes in the spatial dis-

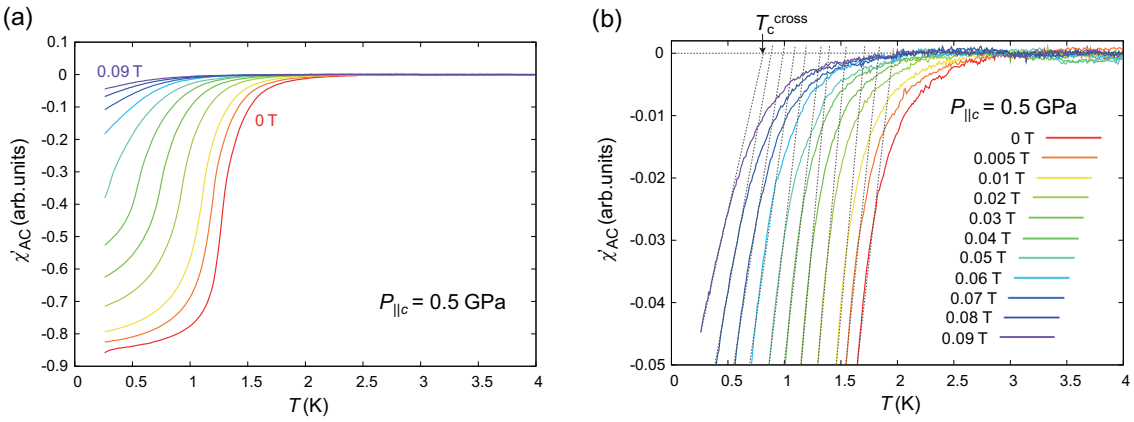

Figure 5.11: Temperature dependence of the real part of the AC susceptibility of Sr_2RuO_4-Ru at $P_{\|c}$ = 0.5 GPa under different H_{DC}'s, measured with $\mu_0 H_{AC}$= 2 μT-rms and f = 293 Hz: (a) the entire behavior and (b) an enlarged view of the $P_{\|c}$-enhanced shielding region.

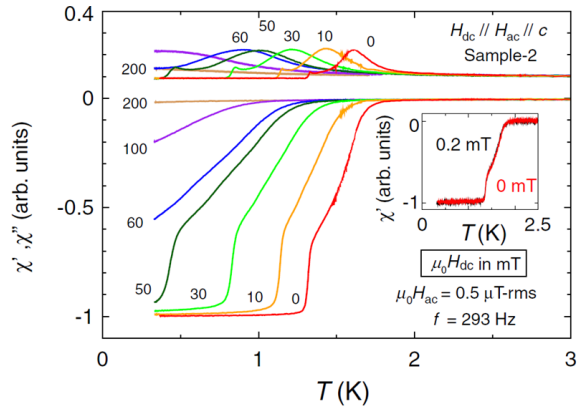

Figure 5.12: Temperature dependence of the AC susceptibility of Sr_2RuO_4-Ru at $P_{\|c}$ = 0 GPa under different H_{DC}'s [31].

tribution of superconducting regions caused by pressure, such as an increase of intergranular distance or a change in the shape of superconducting grains themselves. We note, however, that possibilities of extrinsic origins such as cracks have not been excluded so far.

5.2.3 Resistivity under UAP

In order to obtain a hint to clarify the difference of the spatial distribution between $P_{\|c}$-originated 3-K SC and interfacial 3-K SC, we measured four-wire resistance of Sr_2RuO_4-Ru under $P_{\|c}$(Fig. 5.14). At 0 and 0.3 GPa, only a broad transition is observed. In clear contrast, two transitions, a sharp superconducting transition at about 1.5 K and a broad superconducting transition below about 3 K are observed under 0.1 GPa. This peculiar pressure dependence sug-

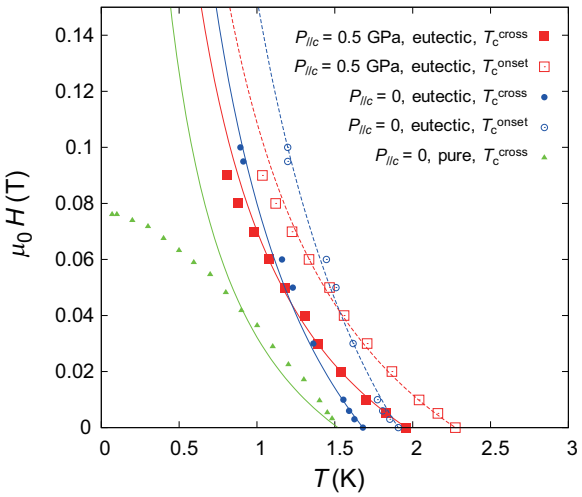

Figure 5.13: Comparison of H-T phase diagrams for $H_{\|c}$ based on two different T_c definitions: T_c^{cross} and T_c^{onset} (see text). Solid and dashed lines indicate fitting curves with Eq. (5.1) for a model of an assembly of intergranular Josephson junctions [87]. These curves reproduce the concave-up behavior of the $P_{\|c}$-originated SC above $P^*_{\|c}$, as well as that of the interfacial SC below $P^*_{\|c}$.

gests that the interfacial 3-K SC formed at 0 GPa is destroyed by $P_{\|c}$ whereas the $P_{\|c}$-originated 3-K SC develops with $P_{\|c}$. At 0 GPa, a superconducting path is formed above the bulk T_c of about 1.5 K by the proximity effect of the interfacial 3-K SC. Under 0.1 GPa, the interfacial 3-K SC is substantially suppressed, while $P_{\|c}$-originated 3-K SC is not yet induced much; as a result, a superconducting path formation is not complete above the bulk T_c and the resistance suddenly drops at bulk T_c. At 0.3 GPa, a superconducting path is formed above the bulk T_c by the proximity effect of the $P_{\|c}$-originated 3-K SC. Non-zero resistance at the base temperature of 0.3 K, which is enough below the bulk T_c is attributable to micro cracks in the sample and indicates that the estimation of resistivity from resistance is difficult. Increase of resistance with pressure suggests that the number of cracks increases by pressure.

5.2.4 Discussion

From the AC susceptibility and resistance measurements mentioned above, we clarified that the $P_{\|c}$-originated 3-K SC is granular-like similarly to the interfacial 3-K SC but their spatial distribution and out-of-plane UAP dependence are different. Based on these findings, we propose pressure evolution of the spatial distribution of SC in Sr_2RuO_4-Ru under $P_{\|c}$ as shown in Fig. 5.15. At 0 GPa, Sr_2RuO_4 regions around the interfaces between Sr_2RuO_4 and Ru exhibit SC at 3 K because of the moderate lattice distortion, these superconducting regions expand on cooling because of the proximity effect, and one complete superconducting path is formed between $V+$ and $V-$ wires above bulk T_c of ambient Sr_2RuO_4 (1.5 K). Under 0.1 GPa, T_c of Sr_2RuO_4 around the interfaces is suppressed because of the too much lattice distortion, and 3-K SC emerges in other regions in which moderate distortion is induced by $P_{\|c}$. The distance bewteen the regions of this

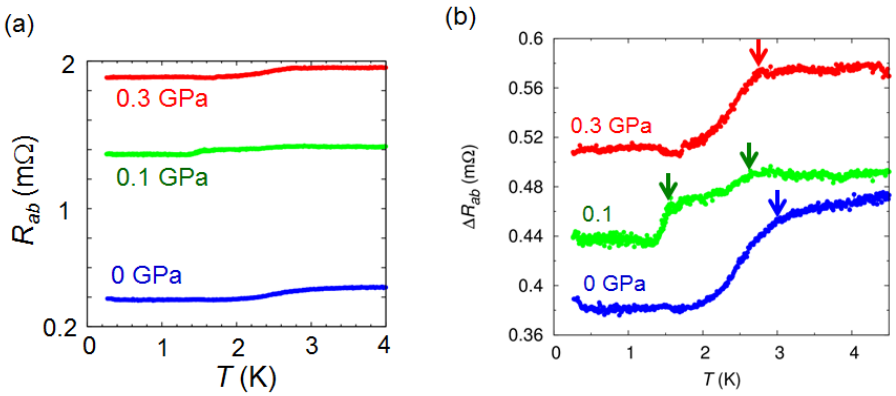

Figure 5.14: Temperature dependence of in-plane resistance of Sr_2RuO_4-Ru under out-of-plane UAP. (a) Raw data. (b) $R(T)$ curves for 0.1 and 0.3 GPa are shifted. Arrows indicate an onset of superconducting transition. Non-zero resistance enough below the bulk T_c is attributable to the cracks of the sample and indicates that the estimation of resistivity from resistance is difficult.

newly-induced 3-K SC is so long that a complete superconducting path cannot be formed by proximity effect above 1.5 K. At 0.3 Pa, the region of the $P_{\|c}$-originated 3-K SC expands and more than one complete superconducting path is formed above 1.5 K, although T_c of interfacial Sr_2RuO_4 is suppressed more. This description is consistent with the results of our previous paper [32].

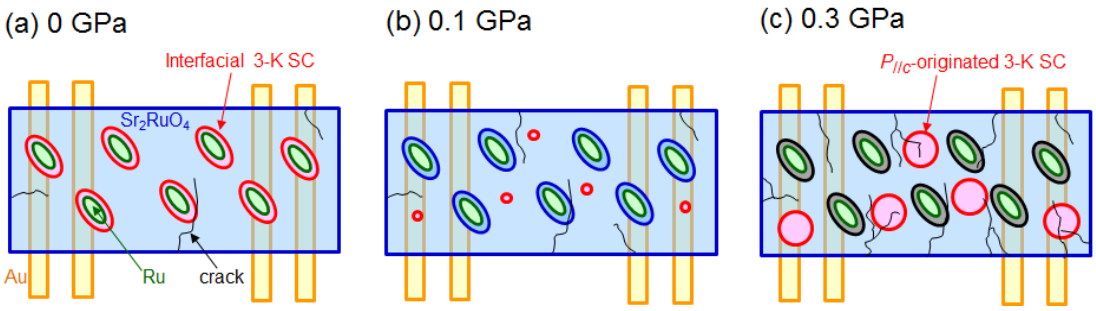

Figure 5.15: Schematic figure of spatial distribution of superconductivity in Sr_2RuO_4-Ru under $P_{\|c}$. (a), (b), and (c) represents the case of 0, 0.1, and 0.3 GPa, respectively. A blue big rectangle denotes a sample of Sr_2RuO_4-Ru, green small ellipses denote Ru lamellae, and yellow thin rectangles denote Au wires attached for resistance measurement. Black lines denote micro cracks. T_c of red, blue, green, and black regions is about 3 K, 1.5 K (bulk T_c of ambient Sr_2RuO_4), 0.49 K (T_c of Ru metal), and 0 K, respectively.

Chapter 6

Summary: Uniaxial pressure effects on Ca_2RuO_4 and Sr_2RuO_4

In this study, we have studied the electronic states of Ca_2RuO_4 and Sr_2RuO_4 under UAPs with three different pressure directions: two in-plane directions, $[100]_T$ and $[110]_T$, and the out-of-plane direction, $[001]_T$, using the tetragonal notation. $[100]_T$ and $[110]_T$ direction are parallel and diagonal to the in-plane Ru-O bond of the RuO_6 octahedra, respectively.

We succeeded in inducing the ferromagnetic metallic (FM-M) phase into Ca_2RuO_4 by in-plane UAPs. The mechanism of this Mott transition is considered to be the same as that under hydrostatic pressure: the out-of-plane flattening distortion of RuO_6 octahedra is released, and the *xy* and *yz*,*zx* bands of Ru 4*d* electrons approach energetically and overlap. The smaller uniaxial critical pressure of the FM-M phase than hydrostatic one demonstrates the advantage of the in-plane uniaxial pressure for changing the electronic state of Ca_2RuO_4. We revealed highly anisotropic pressure-temperature phase diagrams among the AFM and FM phases. The possible absence of the B-AFM phase around the emergence of the FM-M phase under $P_{\parallel[110]T}$ suggests the pressure along the orthorhombic *b* axis induces an electronic state different from those under P_{hydro}.

We clarified that the insulating gap of Ca_2RuO_4 is suppressed from 3000 K to 700 K under out-of-plane UAP. This result is surprising because $P_{\parallel c}$ should increase the crystalline field splitting. This gap suppression is expected to be induced by the enhancement of the band width as a result of the release of rotation or/and tilting distortion of RuO_6 octahedra.

The in-plane UAP effect on Sr_2RuO_4 was also revealed to be significantly anisotropic; we clarified that $P_{\parallel[100]T}$ is more favorable for inducing 3-K superconductivity (SC) than $P_{\parallel[110]T}$. These 3-K SCs under in-plane UAPs are considered to have the superconducting order parameter whose orbital part is one-component and to be induced mainly by elastic distortion.

For out-of-plane UAP effect on Sr_2RuO_4, we newly proposed the pressure dependence of the spatial distribution of 3-K SC in Sr_2RuO_4-Ru based on the behavior of AC susceptibility and resistivity.

To summarize, we have succeeded in inducing several phase transitions in $Ca_{2-x}Sr_xRuO_4$ using UAPs. These results strongly demonstrate the effectiveness of UAP to control the electronic state of systems which have multiple degrees of freedom.

As a future investigation, UAP application to thin film will be interesting for Ca_2RuO_4, because thin film Ca_2RuO_4 is already metallic under ambient pressure and a prominent effect like the emergence of SC is expected under in-plane UAP. For Sr_2RuO_4, in order to clarify the lattice distortion which induces 3-K SC under in-plane UAPs in detail, neutron measurements will be essential.

Acknowledgment

I am grateful to my supervisor, Prof. Y. Maeno for guidance with continuous encouragement. His accurate suggestions have made this study successful.

I appreciate my collaborators' contributions. Prof. S. Yonezawa always gave me detailed discussions and fruitful advices. Thanks to his patient teaching, I was able to establish the whole experimental setup including a LabVIEW program by myself. Prof. H. Yaguchi and Prof. S. Kittaka constructed the initial setup for uniaxial pressure experiments and taught it to me. Prof. F. Nakamura provided Ca_2RuO_4 single crystals with high quality and made various suggestions for resistivity measurement under uniaxial pressure. Prof. S. K. Goh gave me important advices for establishing the technique of the mini-coil AC susceptibility measurement, hosting me kindly during my two-months stay in Cambridge. Mr. R. Ishikawa and Mr. K. Nishimura supported me every day.

I express deep gratitude to all the members of Quantum Materials Laboratory including the former members for having shown me the attitude toward research, told me detailed ways of experiments, given me comments on our results, and helped me as well as shared enjoyable times. Especially, Prof. K. Ishida took care of me, and Mr. T. Hattori, Mr. T. Iye and Mr. T. Yamagishi were good classmates.

I also acknowledge the supports from the LTM center and the machine shop which were necessary to this study.

This work was supported by the "Topological Quantum Phenomena" (No. 22103002) Grant-in Aid for Scientific Research on Innovative Areas from the Ministry of Education, Culture, Sports, Science and Technology (MEXT) of Japan, by a Grant-in-Aid for the Global COE program "The Next Generation of Physics, Spun from Universality and Emergence" from the MEXT of Japan, and by MEXT KAKENHI (No. 25610095). I was supported by JSPS and GCOE Fellowship.

I appreciate my family's warm encouragement. I thank my father also for having given me a chance to have an interest in physics. I am obliged to my mother for her support in every aspect. I am thankful to my dear "children", Ciel and Urara for always being beside me and giving me inexhaustible power and love.

Bibliography

[1] Nakatsuji S, Ikeda S I and Maeno Y 1997 *J. Phys. Soc. Jpn.* **66** 1868

[2] Alexander C S, Cao G, Dobrosavljevic V, McCall S, Crow J E, Lochner E and Guertin R P 1999 *Phys. Rev. B* **60** 8422(R)

[3] Mackenzie A P and Maeno Y 2003 *Rev. Mod. Phys.* **75** 657–712

[4] Maeno Y, Kittaka S, Nomura T, Yonezawa S and Ishida K 2012 *J. Phys. Soc. Jpn.* **81** 011009

[5] Braden M, Andre G, Nakatsuji S and Maeno Y 1998 *Phys. Rev. B* **58** 847

[6] Steffens P, Friedt O, Alireza P, Marshall W G, Schmidt W, Nakamura F, Nakatsuji S, Maeno Y, Lengsdorf R, Abd-Elmeguid M M and Braden M 2005 *Phys. Rev. B* **72** 094104

[7] Nakamura F 2007 *J. Phys. Soc. Jpn.* **76** Suppl. A 96

[8] Nakamura F, Goko T, Ito M, Fujita T, Nakatsuji S, Fukazawa H, Maeno Y, Alireza P, Forsythe D and Julian S R 2002 *Phys. Rev. B* **65** 220402(R)

[9] Alireza P L, Nakamura F, Goh S K, Maeno Y, Nakatsuji S, Ko Y T C, Sutherland M, Julian S and Lonzarich G G 2010 *J. Phys.: Condens. Matter* **22** 052202

[10] Nakatsuji S and Maeno Y 2000 *Phys. Rev. B* **62** 6458

[11] Nakatsuji S and Maeno Y 2000 *Phys. Rev. Lett.* **84** 2666

[12] Friedt O, Braden M, Andre G, Adelmann P, Nakatsuji S and Maeno Y 2001 *Phys. Rev. B* **63** 174432

[13] Nakatsuji S, Hall D, Balicas L, Fisk Z, Sugahara K, Yoshioka M and Maeno Y 2003 *Phys. Rev. Lett.* **90** 137202

[14] Wang X, Xin Y, Stampe P A, Kennedy R J and Zheng J P 2004 **85** 6146

[15] Miao L, Silwal P, Zhou X, Stern I, Peng J, Zhang W, Spinu L, Mao Z and Kim D H 2012 *Appl. Phys. Lett.* **100** 052401

[16] Nakamura F, Sakaki M, Yamanaka Y, Tamaru S, Suzuki T and Maeno Y 2013 *Sci. Rep.* **3** 2536

[17] Okazaki R, Nishina Y, Yasui Y, Nakamura F, Suzuki T and Terasaki I 2013 *J. Phys. Soc. Jpn.* **82** 103702

[18] Woods L M 2000 *Phys. Rev. B* **62** 7833

[19] Fang Z and Terakura K 2001 *Phys. Rev. B* **64** 020509(R)

[20] Hotta T and Dagotto E 2001 *Phys. Rev. Lett.* **88** 017201

[21] Anisimov V I, Nekrasov I A, Kondakov D E, Rice T M and Sigrist M 2002 *Eur. Phys. J. B* **25** 191

[22] Fang Z and Terakura K 2002 *J. Phys.: Condens. Matter* **14** 3001

[23] Fang Z, Nagaosa N and Terakura K 2004 *Phys. Rev. B* **69** 045116

[24] Cuoco M, Forte F and Noce C 2006 *Phys. Rev. B* **74** 195124

[25] Terakura K 2007 *Prog. Mat. Sci.* **52** 388

[26] Gorelov E, Karolak M, Wehling T O, Lechermann F, Lichtenstein A I and Pavarini E 2010 *Phys. Rev. Lett.* **104** 226401

[27] Arakawa N and Ogata M 2012 *Phys. Rev. B* **86** 125126

[28] Arakawa N and Ogata M 2013 *Phys. Rev. B* **87** 195110

[29] Maeno Y, Ando T, Mori Y, Ohmichi E, Ikeda S, NishiZaki S and Nakatsuji S 1998 *Phys. Rev. Lett.* **81** 3765

[30] Ando T, Akima T, Mori Y and Maeno Y 1999 *J. Phys. Soc. Jpn.* **68** 1651

[31] Kittaka S, Nakamura T, Yaguchi H, Yonezawa S and Maeno Y 2009 *J. Phys. Soc. Jpn.* **78** 064703

[32] Kittaka S, Taniguchi H, Yonezawa S, Yaguchi H and Maeno Y 2010 *Phys. Rev. B* **81** 180510(R)

[33] Shirakawa N, Murata K, Nishizaki S, Maeno Y and Fujita T 1997 *Phys. Rev. B* **56** 7890

[34] Forsythe D, Julian S R, Bergemann C, Pugh E, Steiner M J, Alireza P L, McMullan G J, Nakamura F, Haselwimmer R K W, Walker I R, Saxena S S, Lonzarich G G, Mackenzie A P, Mao Z Q and Maeno Y 2002 *Phys. Rev. Lett.* **89** 166402

[35] Sigrist M 2002 *Prog. Theo. Phys.* **107** 917

[36] Agterberg D F 1998 *Phys. Rev. Lett.* **80** 5184

[37] Chmaissem O, Jorgensen J D, Shaked H, Ikeda S and Maeno Y 1998 *Phys. Rev. B* **57** 5067

[38] Longo J M and Raccah P M 1973 *J. Solid State Chem.* **6** 526

[39] Miao L, Zhang W, Silwal P, Zhou X, Stern I, Liu T, Peng J, Hu J, Kim D H and QMao Z 2013 *Phys. Rev. B* **88** 115102

[40] Oguchi T 1995 *Phys. Rev. B* **51** R1385

[41] Singh D J 1995 *Phys. Rev. B* **52** 1358

[42] Matzdorf R, Fang Z, Ismail, Zhang J, Kimura T, Tokura Y, Terakura K and Plummer E W 2000 *Science* **289** 746

[43] Koga A, Kawakami N, Rice T M and Sigrist M 2004 *Phys. Rev. Lett.* **92** 216402

[44] Alireza P L, Barakat S, Cumberlidge A M, Lonzarich G, Nakamura F and Maeno Y 2007 *J. Phys. Soc. Jpn.* **76** Suppl. A 216

[45] Nakamura F, Nakai R, Takemoto T, Sakaki M, Suzuki T, Alireza P L, Nakatsuji S and Maeno Y 2009 *Phys. Rev. B* **80** 193103

[46] Ishida K, Mukuda H, Kitaoka Y, Asayama K, Mao Z Q, Mori Y and Maeno Y 1998 *Nature* **396** 658

[47] K Ishida H Mukuda Y K Z Q M H F and Maeno Y 2001 *Phys. Rev. B* **63** 060507

[48] Duffy J A, Hayden S M, Maeno Y, Mao Z, Kulda J and McIntyre G J 2000 *Phys. Rev. Lett.* **85** 5412

[49] Mazin I I and Singh D J 1997 *Phys. Rev. Lett.* **79** 733

[50] Nomura T and Yamada K 2002 *J. Phys. Soc. Jpn* **71** 1993

[51] Rice T M and Sigrist M 1995 *J. Phys.: Condens. Matter* **7** L643

[52] Allen P B, Berger H, Chauvet O, Forro L, Jarlborg T, Junod A, Revaz B and Santi G 1996 *Phys. Rev. B* **53** 4393

[53] Ishida K, Kitaoka Y, Asayama K, Ikeda S, Nishizaki S, Maeno Y, Yoshida K and Fujita T 1997 *Phys. Rev. B* **56** R505

[54] Mackenzie A P, Haselwimmer R K W, Tyler A W, Lonzarich G G, Mori Y, Nishizaki S and Maeno Y 1998 *Phys. Rev. Lett.* **80** 161

[55] Mao Z Q, Mori Y and Maeno Y 1999 *Phys. Rev. B* **60** 610

[56] Luke G M, Fudamoto Y, Kojima K M, Larkin M I, Merrin J, Nachumi B, Uemura Y J, Maeno Y, Mao Z Q, Mori Y, Nakamura H and Sigrist M 1998 *Nature* **394** 558

[57] Xia J, Maeno Y, Beyersdorf P T, Fejer M M and Kapitulnik A 2006 *Phys. Rev. Lett.* **97** 167002

[58] NishiZaki S, Maeno Y and Mao Z 2000 *J. Phys. Soc. Jpn.* **69** 572

[59] Deguchi K, Tanatar M A, Mao Z, Ishiguro T and Maeno Y 2002 *J. Phys. Soc. Jpn* **71** 2839

[60] Yaguchi H, Akima T, Mao Z, Maeno Y and Ishiguro T 2002 *Phys. Rev. B* **66** 214514

[61] Mao Z Q, Maeno Y and Fukazawa H 2000 *Mater. Res. Bull.* **35** 1813

[62] Yaguchi H, Wada M, Akima T, Maeno Y and Ishiguro T 2003 *Phys. Rev. B* **67** 214519

[63] Mao Z Q, Nelson K D, Jin R, Liu Y and Maeno Y 2001 *Phys. Rev. Lett.* **87** 037003

[64] Kawamura M, Yaguchi H, Kikugawa N, Maeno Y and Takayanagi H 2005 *J. Phys. Soc. Jpn.* **74** 531

[65] Ying Y A, Xin Y, Clouser B W, Hao E, Staley N E, Myers R J, Allard L F, Fobes D, Liu T, Mao Z Q and Liu Y 2009 *Phys. Rev. Lett.* **103** 247004

[66] Sigrist M and Monien H 2001 *J. Phys. Soc. Jpn.* **70** 2409

[67] Okuda N, Suzuki T, Mao Z, Maeno Y and Fujita T 2002 *J. Phys. Soc. Jpn* **71** 1134

[68] Kittaka S, Yaguchi H and Maeno Y 2009 *J. Phys. Soc. Jpn.* **78** 103705

[69] Yaguchi H, Kittaka S and Maeno Y 2009 *J. Phys.: Conf. Ser.* **150** 052285

[70] Kittaka S 2010 Ph. D thesis

[71] Lukefahr H G, Collins J K, Camacho E, Yeager C, MacLaughlin D E, Myers A and Bernal O O 1996 *Rev. Sci. Instrum.* **67** 3642

[72] Nakatsuji S, Ikeda S I and Maeno Y 1997 *Physica C* **282** 729

[73] Nakatsuji S, Dobrosavljevic V, Tanaskovic D, Minakata M, Fukazawa H and Maeno Y 2004 *Phys. Rev. Lett.* **93** 146401

[74] Alireza P L and Julian S R 2003 *Rev. Sci. Instrum.* **74** 4728

[75] Lee J S, Lee Y S, Noh T W, Oh S J, Yu J, Nakatsuji S, Fukazawa H and Maeno Y 2002 *Phys. Rev. Lett.* **89** 257402

[76] Pavarini E, Biermann S, Poteryaev A, Lichtenstein A I, Georges A and Andersen O K 2004 *Phys. Rev. Lett.* **92** 176403

[77] Pavarini E, Yamasaki A, Nuss J and Andersen O K 2005 *New. J. Phys.* **7** 188

[78] Pchelkina Z V, Nekrasov I A, Pruschke T, Sekiyama A, Suga S, Anisimov V I and Vollhardt D 2007 *Phys. Rev. B* **75** 035122

[79] Jung J H, Fang Z, He J P, Kaneko Y, Okimoto Y and Tokura Y 2003 *Phys. Rev. Lett.* **91** 056403

[80] Mizokawa T, Tjeng L H, Lin H J, Chen C T, Schuppler S, Nakatsuji S, Fukazawa H and Maeno Y 2004 *Phys. Rev. B* **69** 132410

[81] Yokoya T, Chainani A, Takahashi T, Katayama-Yoshida H, Kasai M, Tokura Y, Shanthi N and Sarma D D 1996 *Phys. Rev. B* **53** 8151

[82] Ying Y A, Staley N E, Xin Y, Sun K, Cai X, Fobes D, Liu T, Mao Z and Liu Y 2013 *Nat. Commun.* **4** 2596

[83] C. Hicks *et al*., 2013, submitted to Science.

[84] C. Hicks *et al*., 2013, unpublished.

[85] C. Hicks, private communication.

[86] Kittaka S, Nakamura T, Aono Y, Yonezawa S, Ishida K and Maeno Y 2009 *Phys. Rev. B* **80** 174514

[87] Gerber A, Grenet T, Cyrot M and Beille J 1992 *Phys. Rev. B* **45** 5099(R)

[88] Chamaya E V, Tien C, Wur C S and Kumzerov Y A 1996 *Physica C* **269** 313